5-7-2016

Influence of Conducting Carbons on the Capacity Retention of NiO//LiCoO2 and Graphite//LiCoO2 Full Cell Lithium Ion Batteries

mengchen liu
University of Connecitcut, mengchen.liu@uconn.edu

Influence of Conducting Carbons on the Capacity Retention of NiO//$LiCoO_2$ and Graphite//$LiCoO_2$ Full Cell Lithium Ion Batteries

Mengchen Liu

B.S. & B.E., Nankai University & Tianjin University, 2014

A Thesis

Submitted in Partial Fulfillment of the

Requirements for the Degree of

Masters of Science

at the

University of Connecticut

2016

APPROVAL PAGE

Master of Science Thesis

Influence of Conducting Carbons on the Capacity Retention of NiO//$LiCoO_2$ and Graphite//$LiCoO_2$ Full Cell Lithium Ion Batteries

Presented by

Mengchen Liu, B.S., B.E.

Major Advisor _____

William E. Mustain

Associate Advisor_____

Yongku Cho

Associate Advisor_____

Jeffrey R. McCutcheon

University of Connecticut

2016

Acknowledgements

I would like to thank my major advisor Dr. William E. Mustain for all of his help, comments and suggestions on my research from literature collecting to experimental characterization. I learned a lot and went through the complete research process in my master period.

I would like to thank my associate advisors Dr. Jeffrey R. McCutcheon and Dr. Yongku Cho who provided insight and expertise that greatly assisted the research.

I would thank to Alessandro Palmieri for showing me, with great detail, how to do build cells and run the battery experiments, as well as analyze the data. I would also like to thank Xiong Peng, Shuai Zhao and Travis Omasta in our research group for characterization assistance and comments that greatly improved the research process.

I would like to thank all of my course professors for sharing their pearls of wisdom with me during the course of this research.

I would like to acknowledge Ford Motor Company for their funding and Center of Clean Energy Engineering in University of Connecticut for the physical characterization instruments.

Finally, I would like to thank to my family and all of my friends for their strong support on my research and life.

Table of Contents

List of Figures

List of Tables

List of Abbreviations

CE	Coulomb Efficiency
CNTs	Carbon Nanotubes
CB	Conductive Carbon
DEC	Diethyl Carbonate
DMC	Dimethyl Carbonate
ESS	Energy Storage System
EC	Ethylene Carbonate
G5	Graphite
LIBs	Lithium Ion Batteries
LCO	Lithium Cobalt Oxide
NMP	1-Methyl-2-pyrrolidone solvent
PVDF	Polyvinylidene Fluoride

Abstract

Lithium ion batteries are the dominant energy storage system in the market today. Based on its high energy density, power density and ideal cycleability, research on lithium ion batteries has gone through several generations in a short timeframe. However, the constantly increasing demand for this portable energy source, which could be used for hybrid electric vehicles, tablets, computers, phones and even micro-electronics for medical apparatus and instruments, drives the design of next generation materials and designs with improved performance and safety.

In this thesis, the influence of conductivity on Lithium-ion battery half cell capacity retention was investigated with graphite and NiO anodes, and a $LiCoO_2$ cathode, which were fabricated with different amounts of conductive carbon addition. Half cells with more conductive carbon highly improved performance in terms of both energy density and cycleability. The high carbon addition active materials were then used to fabricate graphite/$LiCoO_2$ and NiO/$LiCoO_2$ full cells which showed good performance – especially the NiO/ $LiCoO_2$ full cell which has more than 100 mAh g^{-1} capacity left after 25 cycles. This has not been reported in the literature previously. All active materials and fabricated cells were characterized by X-ray diffraction (XRD), scanning electron microscopy (SEM), cyclic voltammetry and charge/discharge measurements.

Comparing with half cells, full cell fabrication and testing has more difficulties to achieve good performance. Some of the important variables are: cell conductivity, lithium ion source, increased side reactions and cut off voltage. For instance, in half cells, the lithium metal counter electrode is an unlimited lithium source with highest energy density, meaning that small parasitic chemical losses in Li are not observed; however, in full cells there is a finite amount of lithium contained in the cathode

during assembly and full cell performance is therefore very sensitive to this unwanted reactions. Carbon is the most common commercial lithium battery anode material today because of its good conductivity and stability. However, the demands of new automotive and grid-scale applications are driving the need for new materials with higher energy density, but maintain the low cost and reliable safety of existing materials. Metal oxides are a promising alternative class of materials currently under development because of the possibility to achieve more than twice the storage capacity of graphite; however, very little work has been done in the literature regarding metal oxide full cells.

Therefore, the overall objective of this thesis is to develop a methodology for creating stable full cell lithium ion batteries with a metal oxide, NiO, anode and commercial $LiCoO_2$ cathode. Particularly, the effects of the electrode recipe, lower full cell cut off voltage, and capacity match between the anode and cathode on the capacity retention are illustrated.

Chapter 1 - Background and Introduction

1.1 Energy Revolution

From the first Industrial Revolution in the 18th century to today, increasing economic prosperity has always been coupled with the production of energy. From a coffee maker to outer space exploration, from drilling wood to making fire to the use of an air conditioner, people rely on energy to make life better. Since the total energy of an isolated system (i.e. Earth) is constant, humans must find increasingly more efficient methods to transfer energy from nature to benefits people's life, and this involves finding ways to effectively store energy that is available when we are not yet ready to use it.

Today, an overwhelming amount of our energy comes from fossil fuel energy, though solar, hydro, and wind energy are emerging and nuclear energy has been harnessed for decades. Approximately, 68% of today's electrical energy is supplied from fossil fuels: coal (42%), natural gas (21%), oil (5%). 14% of electrical energy comes from nuclear, 15% from hydro, and the remaining 3% from renewable energy technologies.[1] The reliance of modern civilization on fossil fuels has brought enormous wealth, but also irreversible pollution at the same time. Fossil fuels are a finite energy source and distributed unevenly across the planet, which directly or indirectly leads to intra- and inter-state conflicts. Moreover, the amount of a given fossil fuel and its source quality are significantly different based on regional formation conditions. This character means that the cost to harness energy is not homogeneous and/or significant environmental damage can occur during extraction. Some recent examples include injection of water into petroleum beds, or the

possibility of changing local geology leading to more frequent earthquakes, etc. After removal, fossil fuel refining requires additional steps like product separation, purification and side product treatment, which are complicated and energy intense processes.

Additionally, CO_2 emissions from fossil fuel burning are seriously harming our environment. In fact, anthropogenic CO_2 emissions are the most significant factor for global climate change, which is not only causing global warming, but also impacting weather patterns, increasing ocean acidification, and disrupting the plant and animal ecological balance.[2] The weather is becoming more intense and we are facing an increasing number of uncommon natural disasters. We are losing an increasing number of islands because of glacier melting, resulting in ocean level rise and a decrease in the diversity of plant and animal life. [3]

Moreover, the air pollution released from fossil fuel's incomplete burning has caused very poor air quality in cities from smog, especially in eastern Asia, shown in Figure 1.1. From the thermodynamic and kinetics viewpoints, it is very difficult to completely combust fossil fuels, resulting in very small carbon particles that are readily released to atmosphere without efficient filtration system. In recent years, this situation is getting worse, and several strategies have been proposed for short-term control, but none of the solutions that have been implemented to date (i.e. eliminating driving and shutting off power plants during the 2008 Beijing Olympic Games) have been practicial, long-term solutions that solve the problem at its origin.

Figure 1.1. Haze in Eastern Asian, Beijing, China[4]

1.2 Lithium Ion Batteries

1.2.1 Lithium Ion Batteries' overview

To solve the above serious problems, there has been increased attention on developing solar energy, hydro energy, wind energy, nuclear energy and other types of clean energy. As the amount of required energy is rapidly increasing due to emerging economies like China, India, Brazil and Africa, there is increased pressure on scientists and engineers outpace this increased demand with clean energy technologies. Some of these clean energies are intermittent and therefore, an effective storage medium is also needed – and at a scale never seen before on planet Earth.

Lithium-ion batteries have attracted world-wide attention as a highly effective, high energy density energy storage system (ESS) since the first commercial battery was successfully made by SONY in the 1990s[5]. Since then, rechargeable Li-ion batteries (LIBs) have enabled the wireless revolution of cell phones, laptop computers, digital cameras, and tablets that has transformed global communication.[2] The utilization of rechargeable and portable energy storage systems allows for the storage

of energy that is generated from wind or solar, which are among the most abundant and are potentially readily available. Taking the rising interest in the commercialization of hybrid electric vehicles (HEVs) and electric vehicles (EVs) as one example, replacing gasoline combustion with stored battery energy can use as little as one-fourth of the energy of petrol-driven cars per kilometer.[3] Therefore, converting to EV and HEV vehicles can have a significant influence in decreasing global (and local urban) CO_2 (and particulate) emissions.

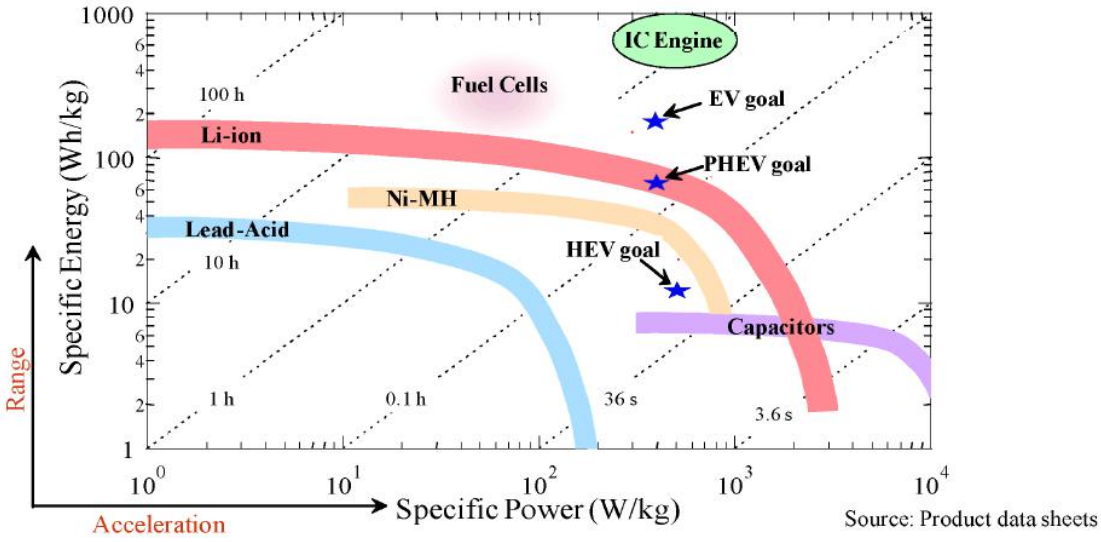

Figure 1.2. Specific Power vs. Specific Energy of varied technologies.[6]

Several factors have contributed to lithium ion batteries emerging as the dominant commercial storage technology. As seen in Figure 1.2 and Figure 1.3, LIBs have both high energy density and high power density. Energy density can be calculated by multiplying the power density (W/kg) with the discharge time (h) = Wh/kg. Lithium ion batteries have much higher specific energy than all other rechargeable batteries, including Pb-acid, NiCd and NiMH batteries. This advantage is rooted mostly in the high LIB operating voltage (around 4V) where the other technologies operate between 1.2-2V.[7] LIBs also have long cycling life and generally reliable safety characteristics, and are also generally low cost.

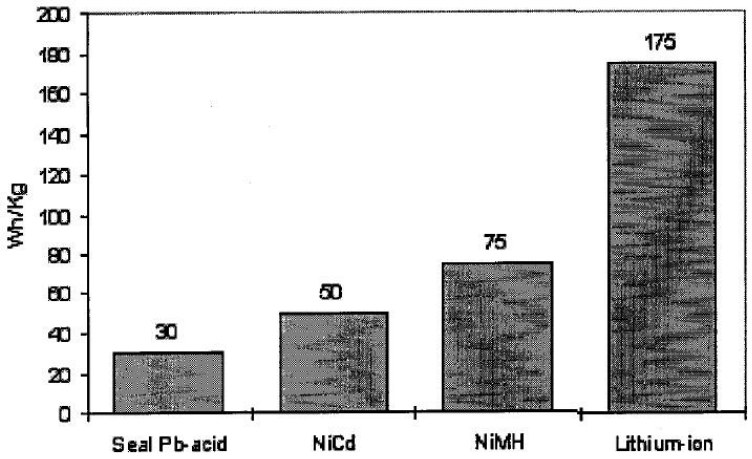

Figure 1.3. Comparison of the specific energy of different types of rechargeable batteries. [8]

1.2.2 Lithium-ion Batteries Mechanism

A lithium-ion battery traditionally consists of a lithium-ion intercalation negative electrode anode like graphite, and a lithium-ion intercalation positive electrode cathode such as $LiCoO_2$ and $LiFePO_4$. The two electrodes are spatially isolated from one another by a separator membrane immersed in lithium-ion conducting electrolyte, almost always 1M $LiPF_6$ in a multi-solvent mixture containing ethylene carbonate (EC), dimethyl carbonate (DMC) and diethyl carbonate (DEC). The solvated lithium ions carry the charge in the electrolyte to complete the electrochemical circuit. The cell configuration and operating principles are shown in Figure 1.4. During the charging process, a lithium ion is extracted from the cathode, i.e. $LiCoO_2$, then transported through the conductive electrolyte and then intercalated into the void volume between the graphene sheets in graphite. Graphite is the most common anode active material used in commercial LIBs. To balance the charge, an electron is carried through the external circuit from $LiCoO_2$ to graphite. This process is electrolytic. The discharging process is spontaneous and the exact reverse from above.

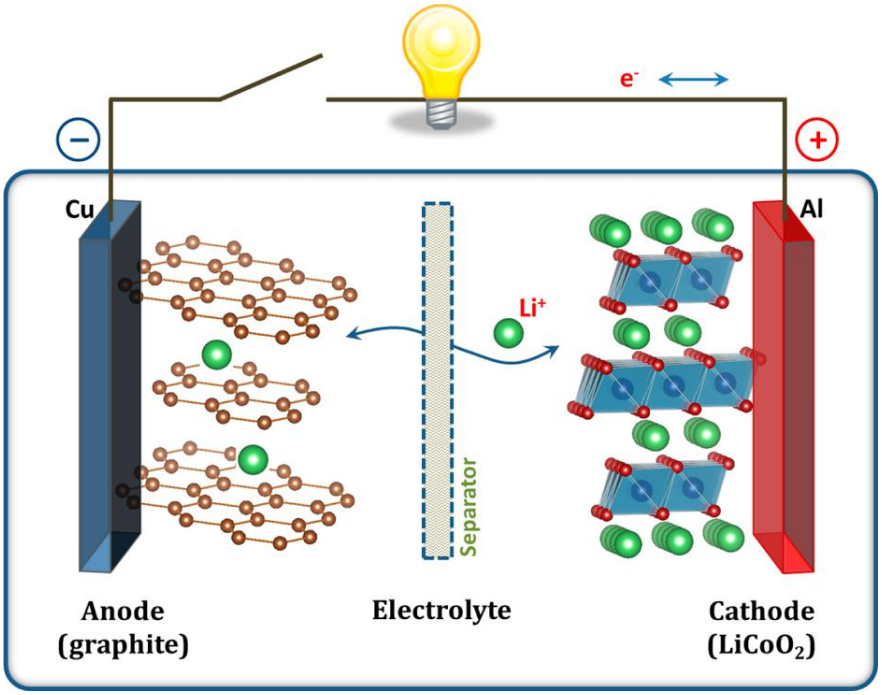

Figure 1.4. Schematic illustration of the charge/discharge process of a typical lithium-ion battery.[2](Reprint with permission from ref. 2. Copyright 2014 Journal of American Society 2013)

The capacity (amount of charge stored per unit mass – typically reported in mAh/g) of these standard anode and cathode materials are not sufficient to meet HEV, EV or grid-scale storage needs. As the result, new anode and cathode materials with higher energy density is needed.

1.2.3 Graphite

Graphite is used in essentially all commercial Li-ion batteries. Graphite, which is highly abundant on earth with low market price, has high external surface area, which can increase the power density. The significant cycleability and conductivity are two additional properties that make graphite attractive. However, graphite has a relatively low low theoretical capacity (372 mAh g^{-1}), which is the primary motivation to find new anode materials with higher capacity.[9] However, cycle life, rate capability and safety cannot be compromised.

1.2.4 Carbon nanotubes and Graphene

Carbon nanotubes and graphene are novel "advanced carbon" anode materials that have shown excellent electrochemical performance in LIBs.[10–16] The theoretical capacity for these advanced carbons are the same as graphite; however, their very high cost limits their application in commercial battery systems. In addition, their theoretical capacity being the same a graphite without a considerable increase in density limits how well they will be used in next-generation LIBs.

1.2.5 Silicon

Silicon is the most commonly used alternative anode material in recent years because of its very high theoretical capacity of 4200 mAh g^{-1}.[17] However, metallurgical Si is very limited in terms of performance because of its significant volume expansion during charging, over 300%. This volumetric expansion leads to very high materials stress and fracturing, hence rapidly and irreversibly degrading the achievable capacity during cycling. This very rapid capacity fade during lithiation and dilithiation has considerably limited the commercial use of silicon in LIB anodes.

Many exotic fabrication methods have been conceived to extend the cycle life of Si anode materials.[11,17–19] In addition to novel nanostructures, carbonation to form Si-C composites and voltage cutoff strategies have been applied. Though these have been somewhat successful in improving Si charge/discharge reversibility, they have limited their achievable capacity to around 700-1000 mAh g^{-1}.

1.2.6 Metal Oxides

In the 700-1000 mAh/g range there are several interesting candidates for LIB anodes, including metal oxides, Figure 1.5. Metal oxides are interesting because not only do they have very high specific (mass-based) capacity, they also have a significantly higher density than both graphite and Si, meaning that much smaller volume batteries can be conceived.

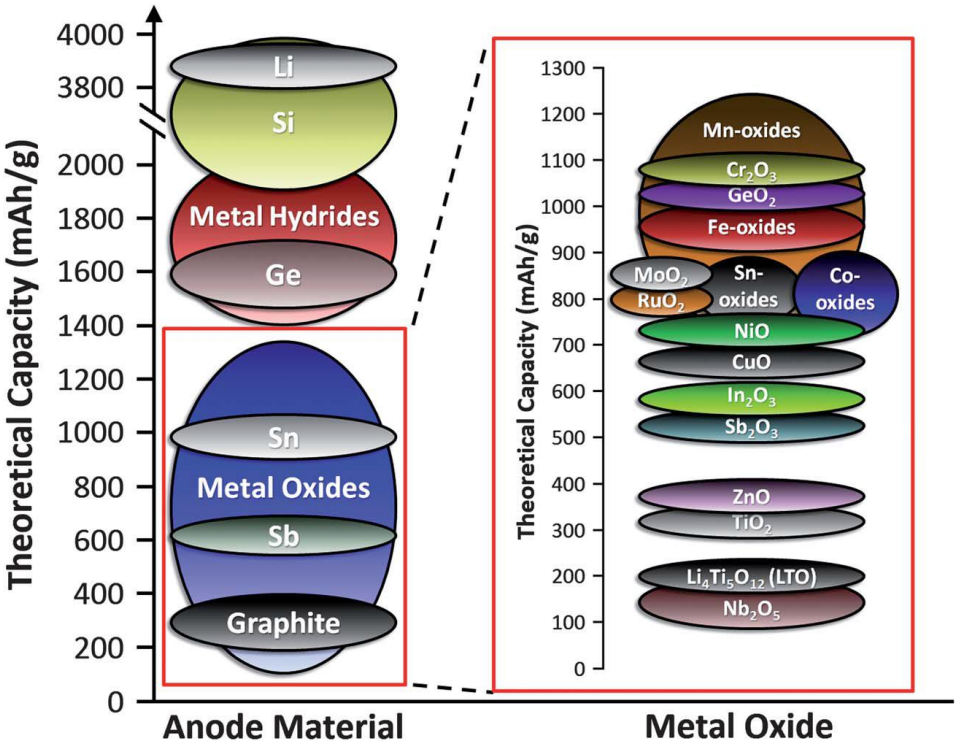

Figure 1.5. Candidate anode materials for lithium-ion batteries and their theoretical capacities.[20](Reprint with permission from ref. 17. Copyright 2014 Journal of Materials Chemistry A)

One possible downside to the use of metal oxides is that their reversible potentials are more positive than graphite by 1-1.5V. Also, metal oxides, like Si anodes, require chemical bonds to be broken during both the charge and discharge. Breaking chemical bonds requires a larger driving force than intercalation, meaning that the electrode overpotentials will be higher than graphite cells as well. This means that the typical operating voltage of a LIB would be reduced to around 2.5-3V instead of ~4V, somewhat limiting the achievable energy and power density. This is less of an issue with energy than power (P=V*i) because of the higher theoretical capacity.

A lot of work on fabricating metal oxide materials in lithium ion batteries has been done by our group in recent years.[20–22] First of all, the influence of conductivity on the capacity retention of NiO anodes in Li-ion batteries was assessed. NiO with different morphologies were synthesized by four different methods using different precursors. The SEM images for these nanostructure is shown in Figure 1.6.[21]

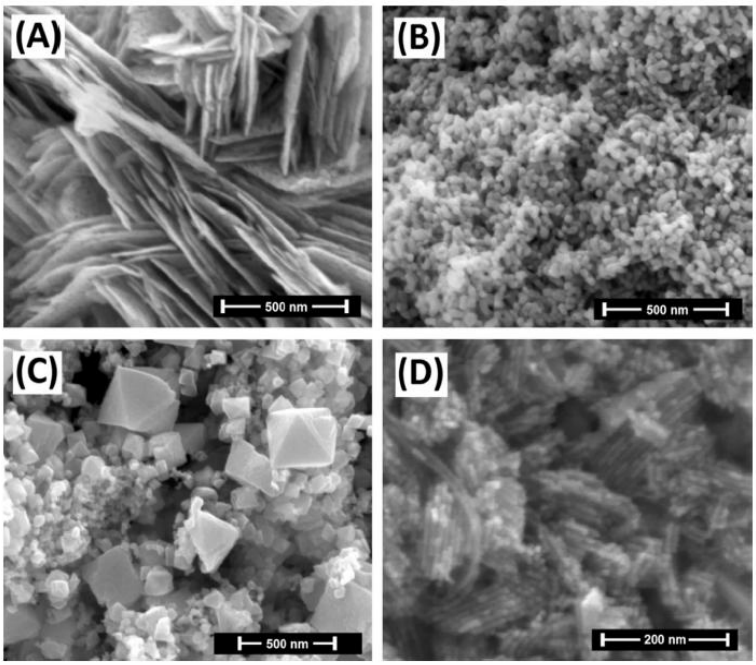

Figure 1.6. SEM images for four different NiO microstructures prepared via different synthesis methods, (A) R-NiO; (B) N-NiO; (C) D-NiO; (D) O-NiO.[18](Reprint with permission from ref. 18. Copyright 2014 Journal of Power Source)

Then, the electronic conductivity of these materials was enhanced systematically by adding a varying amount of conductive carbon to the anode inks. Half cells (active material working electrode and Li foil counter electrode) were fabricated for electrochemical characterization and the capacity retention of the NiO anodes is shown in Figure 1.7.[21] It can be seen that the addition of conducting carbon greatly improved both the achievable capacity and cycleability in all four NiO cases. Through deeper exploration of the formation of the solid electrolyte interphase (SEI) by

shifting features in cyclic voltammograms (CVs) and testing with electrochemical impedance spectroscopy (EIS), it was concluded that the additional carbon played an important role in the SEI formation and the energy density and cycleability.

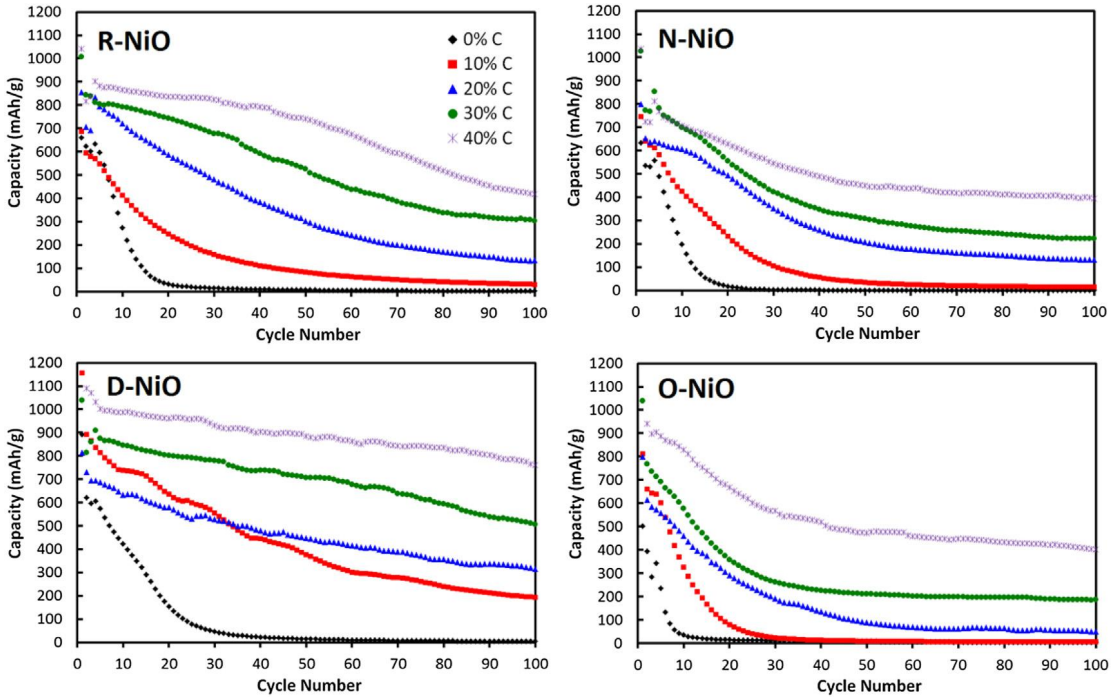

Figure 1.7. Capacity retention plots over 100 cycles at 1C for R-NiO, N-NiO, D-NiO and O-NiO microstructures with increasing carbon content from 0% to 40%.(Reprint with permission from ref. 18. Copyright 2014 Journal of Power Source)

Nanostructural effects on the cycle life and Li^+ diffusion coefficient of NiO anodes was also explored.[22] It was found that that the lithium ion diffusion was impacted by the material nanostructure. Our group also has investigated doping with alkali and transition metals and have introduced advanced carbons (i.e. nanotubes and graphene) into the LIB NiO anode (and other metal oxide chemistries as well). All of these works with NiO anodes provided a strong background to begin the work in this thesis; however, one limitation of the previous work is that our group, and an overwhelming number of the groups studying these materials, had never before tested these NiO anodes in full cells.

1.2.7 Binder

Binders play a critical role in the transformation of active materials into true LIB electrodes. The binder improves particle-to-particle and particle-current collector contact in the cell, making it an integral part of cell assembly. However, the binder is not typically electrically or ionically conductive, meaning that adding excess binder can lower the effective ionic and electronic conductivity, and performance. In this work and in most commercial LIBs, the organic solvent-based Polyvinylidene Fluoride (PVDF) has been used as the anode and cathode binder. PVDF is preferred because of its good electrochemical stability and high adhesion to the electrode materials and current collectors.[23]

Chapter 2 - Experimental Section

2.1 Chemicals and Instruments

Table 2.1. List of chemicals used for LIB preparation.

Chemicals Name	Purity	Company
Graphite	99%	Fisher, Optima
Conductive carbon black	99.5%	IMERYS
1-Methyl-2-pyrrolidone	99.5%	Acros
Isopropanol	99%	Fisher, Optima
Lithium cobalt oxide	99%	Fisher
Coil Cell	Ultra pure	Hohsen Corp
Separator	Ultra pure	Celgard 2320
lithium hexafluorophosphate	98%	Acros
Ethylene Carbonate	99+%	Acros
dimethyl carbonate	98+%	Acros
diethyl carbonate	99%	Acros
Lithium metal	99.9%	Alfa Aesar,
Nitrogen	Ultra pure	Airgas
Argon	Ultra pure	Airgas

Table 2.2. Instrumentation used for cell assembly and characterization.

Instruments Type	Instrument
Mass balance	Fisher scientific instrument
Pipette	Thermal scintifuc
Stir Station	cimarec
Ultrasonicator	Fisher Scientific
Spray gun	Iwata
Vacuum oven	Isotemp
Punch machine	Carver
Calendar	Fisher Scientific
Electrode punch	Fisher Scientific
Separator punch	Fisher Scientific
Glove box	Labconco
Arbin	MSTAT
Vacuum pump	Welch
Scanning Electron Microscopy	FEI Quanta FEG250
X-ray Powder Diffractometer	Bruker
Potentiostat	Autolab PGSTAT302N

2.2 Anode NiO Synthesis

The active material in this experiment was synthesized by another member of Prof. Mustain's group, Neil Spinner, which is a NaOH-induced precipitation (N-NiO). N-NiO was synthesized by preparing an aqueous 0.5M $Ni(NO_3)_2$ solution and quickly adding 10M NaOH while stirring until the pH rose to around 10. The pH was actively monitored using an Accumet Excel XL60 Dual Channel pH/Ion/Conductivity/DO Meter. The solution was then set to rest and covered for 24 hours at room temperature. The precipitate was then rinsed and filtered with excess deionized water, dried overnight in air at 90℃, and calcined in air at 500℃ for 3.5 hours.[21]

2.3 Physical and Electrochemical Characterization

2.3.1 X-ray Powder Diffractometer, XRD

X-ray diffraction (XRD) measurements were carried out using 1.0mm source, 8mm detector slit, Ni filter with a scan rate of 1° min^{-1} from 15° to 80° for NiO and 15°-70° for $LiCoO_2$.

During XRD measurements, the interference between crystal samples' scattered waves cause the diffraction of x-rays. When the angle between the incident x-ray beam and the substrate approaches (2θ) one of the dominant (hkl) indices, this interference increases and x-rays are deflected from the surface to the detector. Thus, the diffraction angle becomes a decisive parameter for the determination of the diffraction line's position and the XRD pattern is simply a one dimensional expression of the material's three dimensional repeated crystal structure. Three important

parameters could be obtained from spectra directly, which are: (1) diffraction peak position (2θ), (2) diffraction peak relative intensity (I), and (3) diffraction peak shape (f(x)). Based on these parameters, a crystalline sample's composition, structure and intermolecular interactions, and other derived information could be determined. Every specific crystal material can be identified with a unique 2θ/d/I set. By the comparison of the obtained data with pure phase XRD peaks in an accepted database or literature, composition, structure, and other qualitative quantitative data can be deduced.

From the XRD pattern, the Sherrer equation (1) can be used to calculate the average grain size. Often, nanoparticles are so small that they do not contain a grain boundary other than their outermost atoms, and very often this calculation is used to determine the average nanoparticle size. A diffraction peak with high intensity, good definition and low neighbor peak interference is preferred. The Line broadening at half the maximum intensity could be calculated by Lorentz function fitting. Then, Equation (1) can be used to calculate average grain size (or nanoparticle diameter).

$$D = \frac{K\lambda}{B\cos\theta} \qquad (1)$$

Where D is the grain size, K is a dimensionless shape factor, always equals 0.89, λ is the x-ray wavelength (0.15406nm here), θ is the Bragg angle and B is the line width at half the maximum intensity (FWHM).[24]

The XRD pattern of as-synthesized N-NiO is shown in Figure 2.1. By comparing with literature, these characteristic peaks are in good agreement with other reported XRD characterizations for NiO materials.[25,26] Five clear and strong diffraction peaks appeared at diffraction angle 37.4°, 43.4°, 63.0°, 75.4°and 79.4°, which corresponds with the (1 1 0), (2 0 0), (2 2 0), (3 1 1) and (2 2 2) fcc crystallite facets.[26]

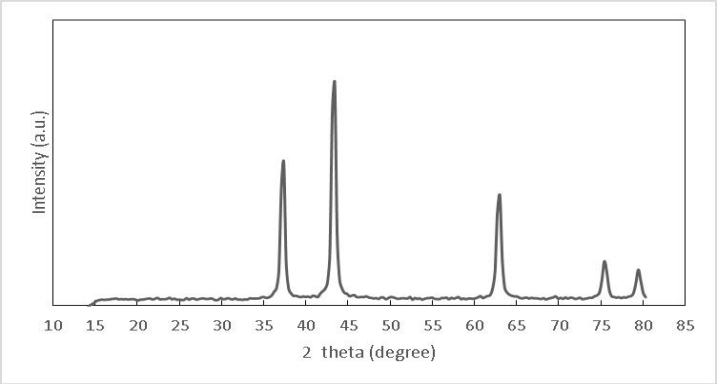

Figure 2.1. XRD patterns of sythesized NiO.

The XRD pattern of the commercial $LiCoO_2$ used in this thesis is shown in Figure 2.2. Comparing with literature, the characteristic peaks are in good agreement with other reported XRD characterizations for $LiCoO_2$ materials.[27,28] Eight clear and strong diffraction peaks appeared at diffraction angles 18.9°, 37.4°, 45.2°, 49.4°, 59.6°, 65.4°, 66.4° and 69.7°which corresponds with (0 0 3), (1 0 1), (1 0 4), (0 1 5), (1 0 7), (0 1 8), (1 1 0) and (1 1 3) crystallite structure which would be illustrated in chapter 3.

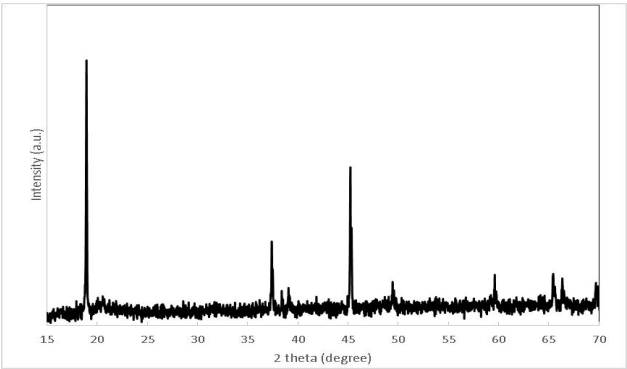

Figure 2.2. XRD patterns of received $LiCoO_2$.

2.3.2 Cyclic Voltammetry (CV) Characterization

Cyclic voltammetry is widely used in electrochemical labs to locate the potentials for redox processes. In cyclic voltammetry, the electrode potential is swept at a known scan rate to a vertex, and then reversed. During a CV measurement,

when the applying potential goes higher than the Nernst potential, the anodic oxidation reaction is accelerated resulting in higher current. The increased reaction rate is accompanied by a decreased number of reactants and increased number of products surrounding the electrode, causing the current to decrease gradually. These dynamics will appear as a peak on CV curves. For a reversible electrode reaction, a pair of peaks will be found from the CV curve, corresponding with an oxidation and reduction peak (negative of the Nernst potential), respectively.

In this thesis, CV tests were run using an Arbin MSTAT battery test station at room temperature. The voltage window was 0.001-1V, 0.001-3V, 2.5-4.2V, 0.001-4.2V and 1.2-4.2V for G5 half cell, NiO half cell, $LiCoO_2$ (LCO) half cell, G5/LCO full cell and NiO/LCO full cell, respectively.

2.3.3 Galvanostatic Cycling test

In this thesis, all half cell and full cell were galvanostatically cycled in Arbin instrument between specific voltage window at room temperature. This this method, a constant current is either applied or extracted until a threshold voltage is achieved. The use of a constant current makes it very easy to calculate the capacity of a material during discharge since it is simply the multiple of the current and time and dividing by the electrode active material mass, giving the unit (mAh/g). The charge and discharge performance were used for capacity retention, energy density and power density evaluation. [9]

2.3.4 Scanning Electron Microscopy, SEM

Scanning Electron Microscopy (SEM) was mainly used for visual characterization of material microstructure. During testing, the SEM instrument measures the emission

of primary electrons; secondary electrons emitted from the sample surface and scattered electrons. This information can then be transformed and deconvoluted into two-dimensional images. Then, the sample material's grain size, morphology, crystallization and uniformity can be determined.[29]

In this thesis, the NiO and LCO microstructure were characterized through SEM analysis; NiO is shown in Figure 2.3. The N-NiO was comprised of nanospheres of nearly uniform size.

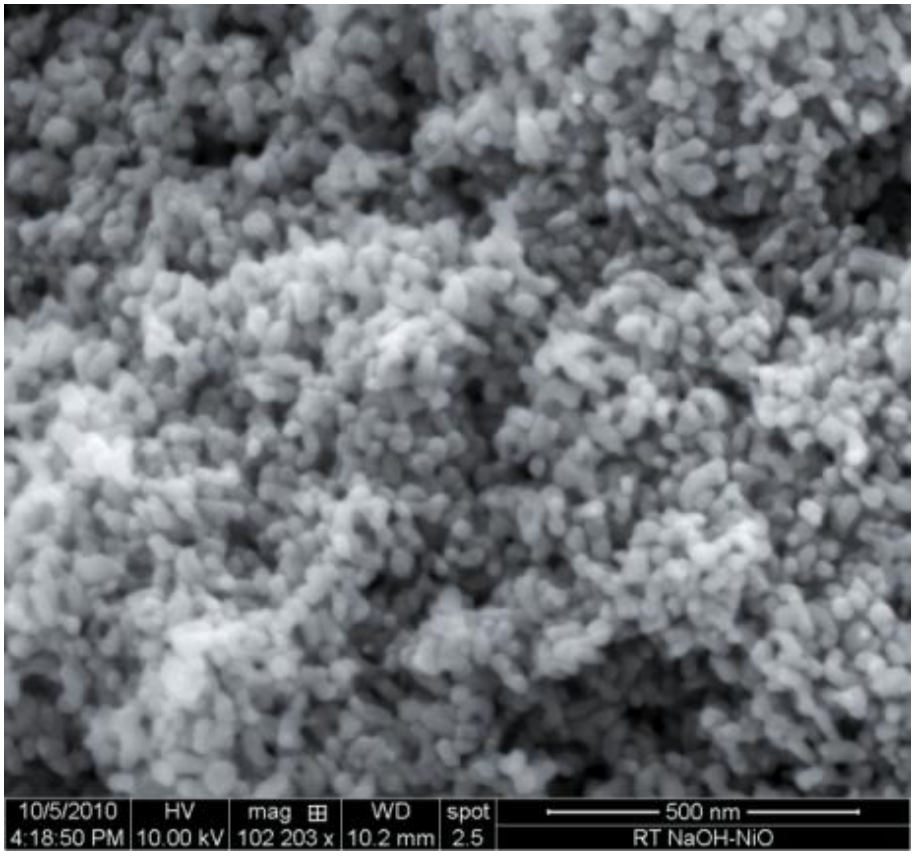

Figure 2.3. SEM images of synthesized NiO.

2.4 Electrode Fabrication

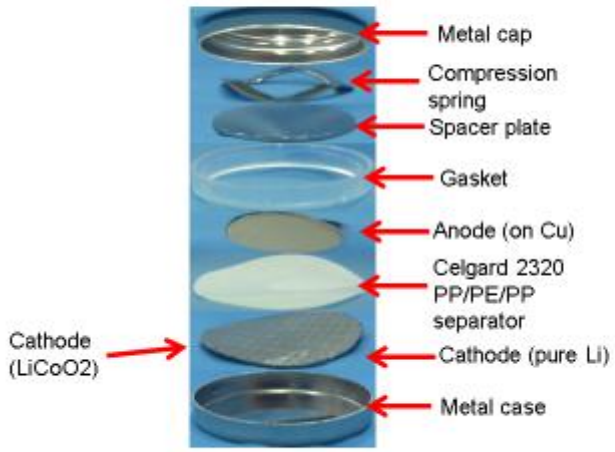

33

Figure 2.4. Coin type cell elements.

2.4.1 Anode Fabrication

Anode electrodes, 1.5cm diameter, consist of active material which were graphite and nickel oxide (NiO) separately, as well as different amounts of conductive carbon black (CB), and polyvinylidene fluoride binder (PVDF) with ratios of 80:10:10 or 50:40:10. Then, a certain amount of 1-Methyl-2-pyrrolidone (NMP) solvent was added to obtain a homogenous and slightly viscous slurry. Then, a uniform solution was achieved by repeated and successive sonication and mechanical stirring overnight. The anode electrode was prepared by spraying the ink with an artist hand spray gun onto the current collector, which was a copper (Cu) foil that had been mechanically roughened and rinsed with isopropanol (IPA). The uniform thickness

anode ink on the copper current collector was heated under vacuum at 120℃ overnight, then pressed at 1500 lbs and massed to obtain the loading. For all electrodes fabricated in this study, the active loading was kept below 2 mg/cm^2.

2.4.2 Cathode Fabrication

The cathode fabrication was similar to the anode fabrication. Cathode electrodes with 1.5cm diameter were comprised of active material, which was lithium cobalt oxide (LCO), CB and PVDF by 80:10:10 and 50:40:10. Then, a certain amount of NMP was added to obtain a homogenous and slightly viscous slurry. Then a uniform ink was achieved by repeated and successive sonication and mechanical stirring overnight. The cathode electrode was prepared by spraying the ink with an artist spray gun onto the current collector which was aluminum (Al) foil that had been rinsed and cleaned with IPA. The uniform thickness cathode ink on the aluminum current collector was heated in a vacuum oven under 120℃ overnight, then pressed at 1500 lbs and massed to obtain the loading. For all of the cathode electrodes fabricated in this study, the active loading was kept below 2 mg $LiCoO_2$/cm^2.

2.5 Coin Cell Assembly

2.5.1 Half cell Coin Cell Assembly

Coin cells were constructed to test graphite and NiO anodes, and LCO cathodes in half cell configuration separately. The hardware used for all of the half cell tests were 2.0 cm diameter Hohsen coin cells, lithium metal counter electrode, and one 1.9 cm diameter Celgard 2320 tri-layer PP/PE/PP separator, one spacer disk, one disk spring and one gasket. The electrolyte was 1 M lithium hexafluorophosphate ($LiPF_6$) solution in ethylene carbonate (EC), dimethyl carbonate (DMC) and diethyl carbonate (DEC) with 1:1:1 volume ratio. In the glove box filled with Argon gas, 15 μL of electrolyte was pipetted onto each side of the separator (30 μL in total), anode and lithium metal were set in sequence, then pressed and sealed into coin cell hardware. In the end, the coin cell was removed from glove box and used for electrochemical characterization at room temperature.

2.5.2 Full cell Coin Cell Assembly

Full cell assembly was similar to the half cell assembly. Coin cells were constructed to test G5/LCO and NiO/LCO in full cell configuration. The materials used for both G5/LCO and NiO/LCO full cell were 2.0 cm diameter coin cells. G5 graphite and NiO were used as the anode electrode separately. LCO was the only cathode electrode that was used. To assemble full cells, two 1.9 cm diameter Celgard 2320 tri-layer PP/PE/PP separators, one spacer disk, one disk spring and one gasket were used. The electrolyte was 1 M $LiPF_6$ solution in EC, DMC and DEC with a 1:1:1 volume ratio. In the glove box filled with Argon gas, 15 μL of electrolyte was pipetted onto each side of the separator (30μL in total); the anode and cathode were

set in sequence then pressed and sealed into coin cell hardware. Finally, the coin cells were removed out from the glove box and used for electrochemical characterization.

2.6 Electrochemical Characterization

2.6.1 Anode and Cathode half cell Characterization

The assembled half cell for graphite and NiO anode materials were galvanostatically cycled between 0.001-1 and 0.001-3 V separately at a constant C-rate of C/5 (or 0.2 C). The current value calculation was based on the theoretical capacity for graphite and NiO which are 372 mAh g^{-1} and 718 mAh g^{-1}, respectively. The assembled $LiCoO_2$ half cells were galvanostatically cycled between 2.5 and 4.2 V at C/5 rate. The cathode current value calculation was based on the theoretical capacity for $LiCoO_2$ which is 274 mAh g^{-1}.

2.6.2 G5/LCO and NiO/LCO full cell Characterization

The assembled G5/LCO and NiO/LCO full cells were galvanostatically cycled between 0.01-4.2V and 1.2-4.2V, respectively, at a constant C/10 rate, which is 0.1 C.[9,19,24,30–35] The C-rate calculation was based on the theoretical capacity for $LiCoO_2$ which is 274 mAh g^{-1}. The cathode was used to calculate the cell capacity since it was always the limiting reactant.

For full cell testing, the capacity match between the anode and cathode is important. The electrodes active loading was controlled based on the calculation of the active material's real capacity after 50 cycles (in the half cell experiments) which were 300 mAh g^{-1} for graphite, 400 mAh g^{-1} for NiO and 140 mAh g^{-1} for LCO. To make sure that cathode electrode could be fully reacted, the anode capacity should slightly exceed that of the cathode electrode.

In this thesis, the active loading (in one embodiment) for the NiO anode, G5 anode and LCO cathode were 0.2045 mg/cm^2, 0.2893 mg/cm^2 and 0.5335 mg/cm^2, respectively. Then:

- NiO Anode Capacity=0.2045 mg/cm^2 (active load) * 400 mAh g^{-1}(energy density) * constant area =82.16 * constant area
- G5 Anode Capacity=0.2893 mg/cm^2 (active load) *300 mAh g^{-1}(energy density)* constant area =86.79*constant area
- LCO Cathode Capacity=0.5335 mg/cm^2 (active load) *140 mAh g^{-1}(energy density) * constant area =74.69*constant area

For NiO//LCO full cell:

- NiO Anode capacity : LCO Cathode capacity= 82.16:74.69=1.10
- For G5//LCO full cell:
- G5 Anode capacity : LCO Cathode capacity= 86.79:74.69=1.16

It is supposed that the cathode electrode could be completely reacted since the anode capacity was slightly larger than the cathode electrode. As a result, the current was calculated based on the LCO cathode loading which was:

- C/10 Current = 0.5335 (LCO Active Loading)*1.76(Cell area)*10^{-6}(units conversion)*274 (LCO Theoretical Capacity)/10(rate) = 0.00002573 A

All charge and discharge electrochemical experiments were conducted using an Arbin MSTAT battery test station at room temperature.

Chapter 3 Results and Discussion

3.1 Graphite Anode Half Cells

Based on the literature, it is expected that ordered carbons such as graphite would have excellent cycleability as an anode material. Graphite anode half cells were fabricated and tested.

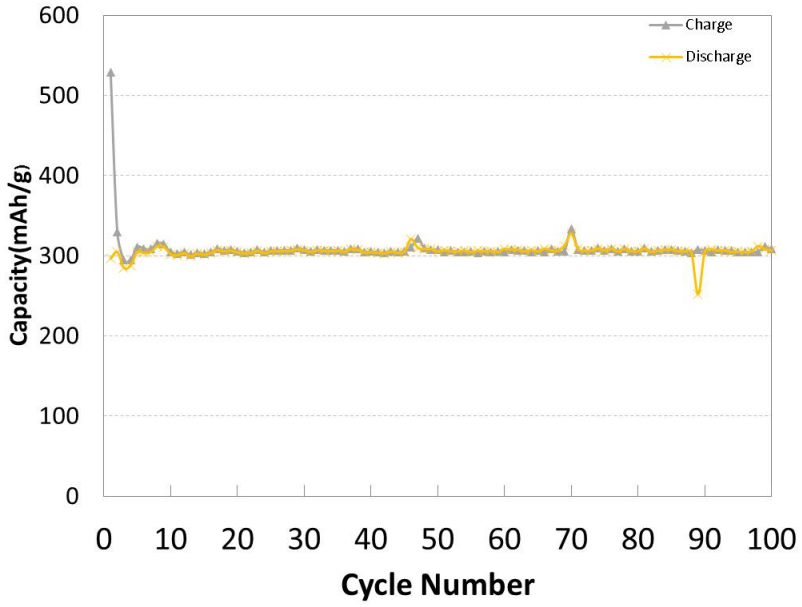

Figure 3.1. Capacity fade of the half-cell employing Graphite:CB:PVDF=80:10:10 electrode as anode between 0.001 and 1V $V_{Li+/Li}$ at C/5 rate.

As shown in Figure 3.1, the cycleability for graphite anode half cell with 10% of conductive carbon was very good. In the first cycle, the charge capacity was 529 mAh g^{-1} with a discharge capacity of 296 mAh g^{-1}. The large capacity fade is caused by the formation of the solid electrolyte interphase (SEI), and this capacity loss is irreversible. However, from the second cycle to the 100^{th} cycle, the charge and

discharge capacity were almost the same around 305mAh g^{-1}, which corresponds to a coulombic efficiency of around 100%.

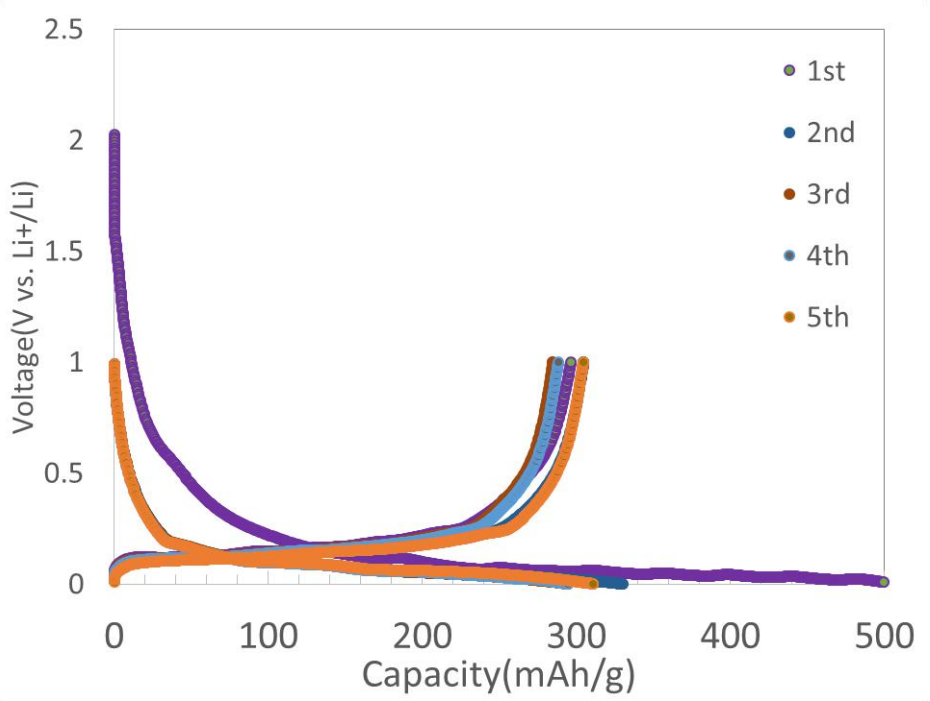

Figure 3.2. Voltage-capacity curves of the half-cell employing Graphite:CB:PVDF=80:10:10 electrode as anode between 0.001 and 1V $V_{Li+/Li}$ at C/5 rate.

Figure 3.2 shows the voltage-capacity charge-discharge curves of a representative G5 anode half cell employing 10% of conductive carbon black. Each of these curves was represented as a single date point in Figure 3.1. As expected, the voltage profile is generally flat and there is very little hysteresis between the charge and discharge voltages.

3.2 NiO Anode Half Cells

Today's urgent demands for lithium ion batteries include the improvement of energy density and power density. As mentioned above, metal oxides, and NiO in particular, have the potential to increase both. One advantage of the NiO

nanospheres in Figure 2.3 is that they have a very small lithium ion diffusion distance, which is expected to help with the discharge rate and reaction reversibililty.[32]

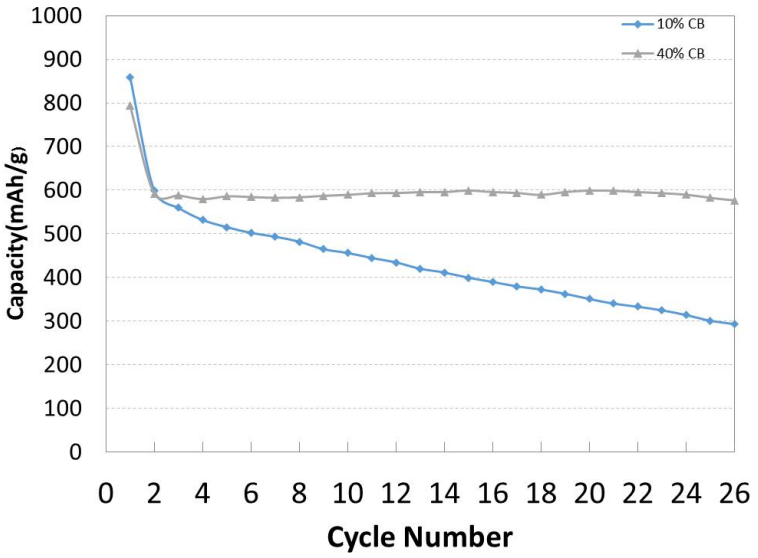

Figure 3.3. Capacity retention plots at C/5 for NiO anode half cell with two different carbon content from 10% to 40%.

Figure 3.3 shows the conductivity effect on the capacity retention of NiO half cells with different amount of carbon addictive. It can be clearly seen that both energy density and cycleability were improved dramatically when the carbon content was increased to 40% from 10%. For the NiO anode half-cell with 10% carbon, the charge capacity dropped steadily from the first cycle to the 25th cycle, where the charge capacity was only 301.0 mAh g^{-1}. This was a significant decrease from the 2nd cycle (after the SEI formation and irreversible capacity loss) where the capacity was 632.5 mAh/g. On the other hand, following the SEI formation, the capacity of the 40% of carbon electrode was nearly unchanged, ending at 582.7 mAh g^{-1} after 25 cycles. It is obvious that conductive carbon addition leads to both better energy density and also cycleability. For 40% carbon black NiO half cell, the irreversible capacity loss was also less than the 10% carbon sample, suggesting that increasing the amount of carbon

impacts SEI formation. Meanwhile, carbon might also help to maintain the electrode microstructure, as well as influence the NiO's structural transformation during charge/discharge.[20] It should also be noted that the additive carbon will not store a significant amount of charge alone, and cannot be independently responsible for the capacity increase observed.

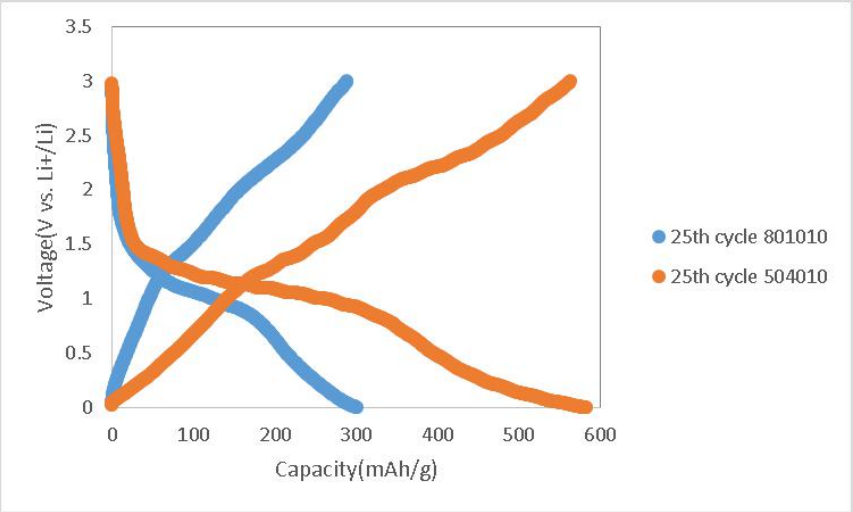

Figure 3.4. The 25th cycle Voltage-capacity curves of the half-cell employing NiO:CB:PVDF=80:10:10, NiO:CB:PVDF=50:40:10 electrodes as anode between 0.001 and 3V $V_{Li+/Li}$ at C/5 rate.

Figure 3.4 shows the 25th cycle's voltage-capacity charge-discharge data for the NiO anode half cell with 10% and 40% carbon. For the NiO anode half-cell with 10% carbon, the charge and discharge capacity was 301.0 mAh g^{-1} and 288.7 mAh g^{-1} which corresponds to a coulombic efficiency of 95.9%. The NiO anode half-cell with 40% of carbon had a much higher capacity of 582.7 mAh g^{-1} for charging and 563.1 mAh g^{-1} for discharging, leading to a coulombic efficiency of 96.6%. Comparing the shape of two voltage-capacity curves, both of them have similar shape with two easily identifiable plateaus at 2.25V and 1V, which corresponds to the NiO conversion

reaction. The NiO anode with 40% carbon did show a more flat plateau during discharge, suggesting improved reaction kinetics.

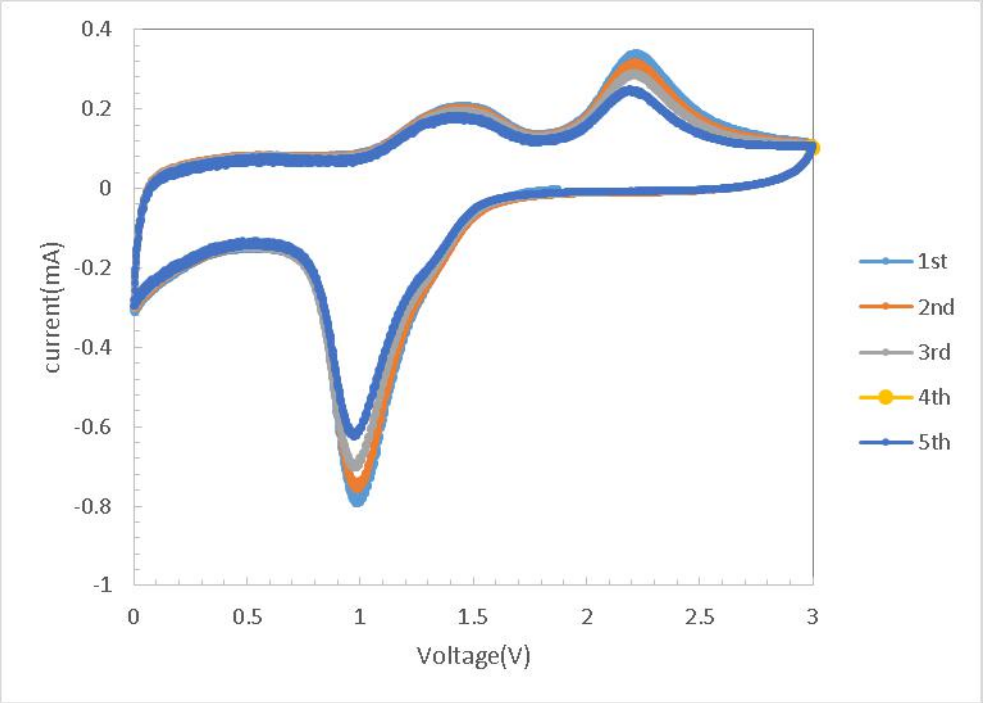

Figure 3.5. Cyclic Voltammograms plot for NiO anode half-cell with NiO:CB:PVDF=80:10:10 ratio obtained at 0.1mV/s from 0.001 to 3 V vs. $V_{Li^+/Li}$.

To determine the oxidation/reduction reactions occurring during NiO anode half-cell tests, the CVs were collected in this configuration. Figure 3.5 presents the cyclic voltammogram for a NiO anode half-cell with NiO:CB:PVDF=80:10:10 ratio obtained at 0.1mV/s from 0.001 to 3 V vs. Li/Li^+. From the Figure 3.5, it can be seen that the first five cycles have good agreement with regards to shape and peak position. In more detail, there are two pairs of redox peaks on the CV curves. The primary peaks were observed at 2.3V and 1V, which are corresponding with oxidation and reduction reactions were related with lithium ions' extraction and insertion respectively for NiO active material. The minor pair of peaks presenting at 1.4V and

0V are likely corresponding with oxidation and reduction reactions for conductive carbon in the electrode.

3.3 LiCoO2 cathode Half Cells

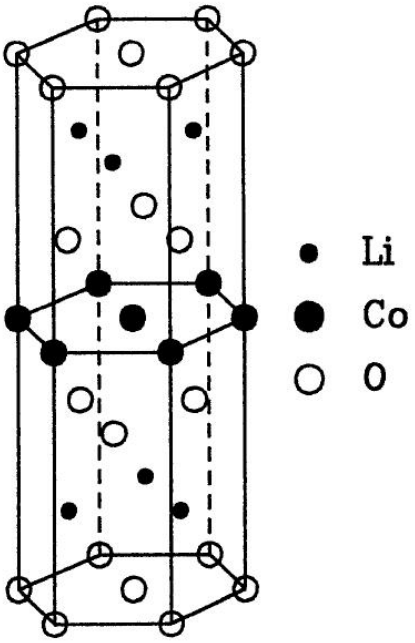

Figure 3.6. $LiCoO_2$'s layer crystal structure which is …ABCABC… stacking of the O-Li-O-Co-O-Li-O layers.[36](Reprint with permission from ref. 34. Copyright Journal of Electrochemical Society)

$LiCoO_2$ has historically been the most common cathode material used in commercial lithium ion batteries. As shown in Figure 3.6, lithium cobalt oxide ($LiCoO_2$) has layered crystal structure which is composed of O-Li-O-Co-O-Li-O layers. The insertion and extraction of lithium ions facilitate the oxidation and reduction of the Co anion between the (III) and (IV) states during the electrochemical charge and discharge processes. When the lithium ion is extracted from $LiCoO_2$, the Co^{3+} was oxidized to Co^{4+} which is a very unstable oxidation state. As the concentration of Co^{4+} increases, the crystal structure of $LiCoO_2$ can be compromised, possibly leading to irreversible capacity loss in a constructed battery.[36]

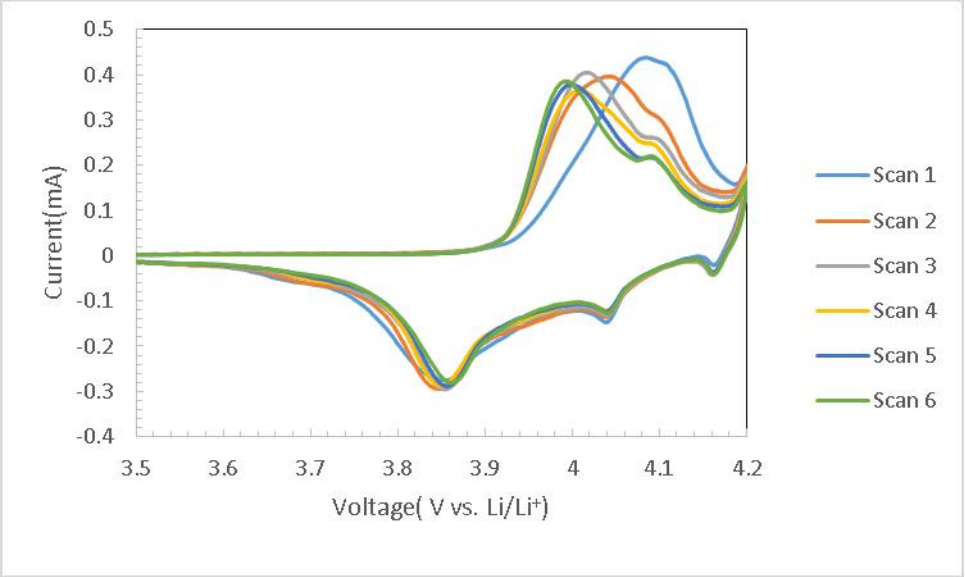

Figure 3.7. Cyclic Voltammograms plot for $LiCoO_2$ cathode half-cell with $LiCoO_2$:CB:PVDF=50:40:10 ratio obtained at 0.1mV/s from 3 to 4.2 V vs. $V_{Li^+/Li}$.

To evaluate and confirm the oxidation and reduction reactions in $LiCoO_2$ cathode half-cells, CVs were performaned on $LiCoO_2$ cathode half-cell with lithium metal serving as the counter electrode. Figure 3.7 shows the cyclic voltammograms for $LiCoO_2$ cathode half-cell with $LiCoO_2$:CB:PVDF=50:40:10 ratio obtained at 0.1mV/s from 3 to 4.2 V vs. $V_{Li^+/Li}$. From Figure 3.7 it can be observed that for the first cycle, there was one major peak at 4.1V and one smaller peak at 4.12V in forward scan. At the same time, three minor peaks appear at voltage 3.86V, 4.05V and 4.18V in the reverse scan. As for the other five cycles, from the second to the sixth cycle, the most significant major peak starts slightly earlier each cycle located at 4.06V, 4.04V, 4.02V, 4.01V and 4V respectively. The areas of those peaks are similar, but slightly smaller than the first cycle. Meanwhile, the smaller major peak became more distinct. However, the minor peaks were very consistent from cycle to cycle without much change in magnitude or position. To illustrate the major peak's difference between the first cycle and other five cycles, it could be noted that delay in the major peak and

higher oxidation current should be attributed to the formation of solid electrolyte interphase. Literature concerning the CV characterization of $LiCoO_2$ cathode half-cell in other papers points to the major oxidation peak at 4-4.1V corresponding to lithium ion (Li^+) extraction. The corresponding reduction peak at 3.86V has been linked to the lithium ion (Li^+) insertion.[37] The three additional, smaller, oxidation and reduction peaks located at 4.05V, 4.18V and 4.12 V can be connected with phase transformation. For the electrochemical mechanism of the $LiCoO_2$ cathode, the lithium ion's deintercalated movement facilitates the formation of Li_xCoO_2 which corresponding with the oxidation and reduction reactions.[36]

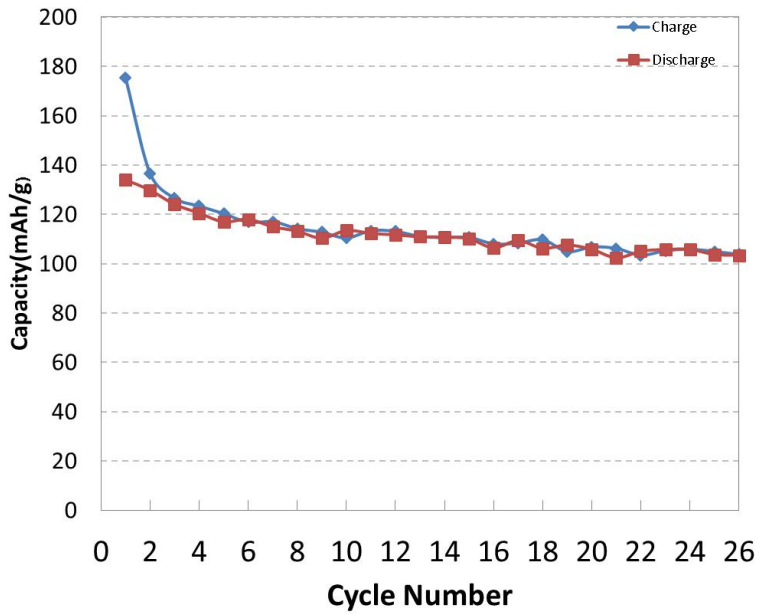

Figure 3.8. Capacity fade of the half-cell employing $LiCoO_2$:CB:PVDF=80:10:10 electrode as cathode between 2.5 and 4.5V $V_{Li+/Li}$ at C/5 rate.

Figure 3.8 shows the cycle performance of the $LiCoO_2$ cathode half-cell at a current density of C/5 between 2.5 and 4.5 V. The discharge capacity of $LiCoO_2$ drops from 134 mAh g^{-1} to 130 mAh g^{-1} in the second cycle which has a small fade considering the effect of electrolyte decomposition. After the 10^{th} cycle, the charge

and discharge capacity fade slowly until the 40th with capacity around 100 mAh g^{-1}. The discharge capacities in the first, 2nd, 10th, 20th, 26th, 40th and 50th cycles are 134, 130, 114, 106, 103, 100, and 90 mAh g^{-1}, respectively.

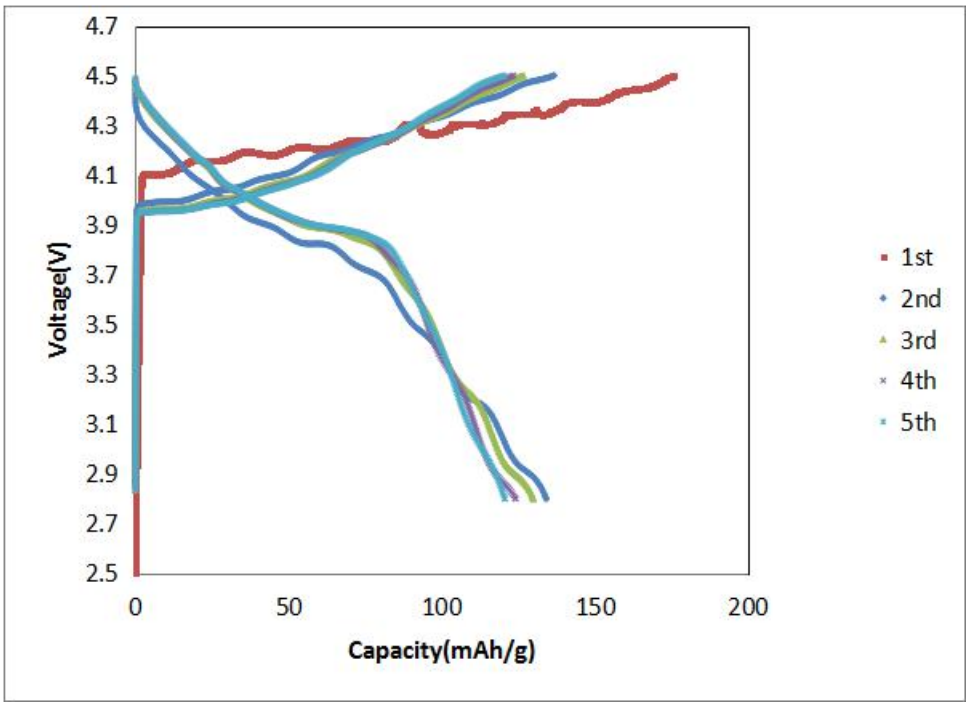

Figure 3.9. Voltage-capacity curves of the half-cell employing $LiCoO_2$:CB:PVDF=80:10:10 electrode as cathode between 2.5 and 4.5V vs. $V_{Li^+/Li}$ at C/5 rate.

Figure 3.9 displays the charge-discharge curves showing the first five cycles lithiation and delithiation behavior of a $LiCoO_2$ half cell. During the first cycle, the half-cell of the $LiCoO_2$ showed an initial irreversible capacity loss of 23.60%, and coulombic efficiency (CE) of 76.40% as the capacity decreased from 175 to 134 mAh g^{-1}. Starting with the 2nd cycle, the irreversible capacity loss was much lower, only 4.95%, yielding a coulombic efficiency of 95.05%. The charge capacity decreased from 175 to 137 mAh g^{-1}, but the capacity was sustainable from the second to fifth cycle. The capacity varied between 120 and 106 mAh g^{-1} out to the 25th cycle as shown in Figure 3.8, where the coulombic efficiency (CE) was always between 97% and 100%.

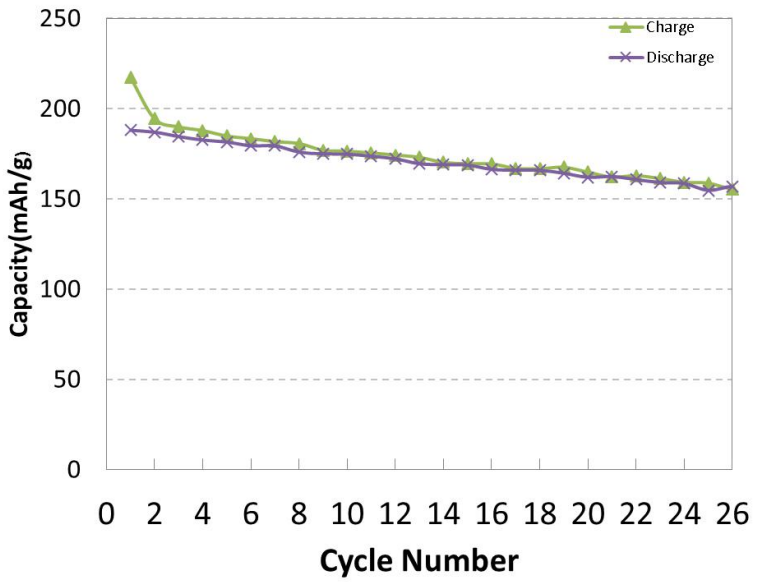

Figure 3.10. Capacity fade of the half-cell employing $LiCoO_2$:CB:PVDF=50:40:10 electrode as cathode between 2.5 and 4.5V $V_{Li+/Li}$ at C/5 rate.

Figure 3.10 shows the cycle performance of the $LiCoO_2$:CB:PVDF=50:40:10 cathode half-cell at a current density of C/5 between 2.5 and 4.5 V. Comparing with the $LiCoO_2$:CB:PVDF=80:10:10 electrode's cathode half cell data, the $LiCoO_2$ cathode electrode half cell delivers higher charge and discharge capacity with more stable cycleability. In the first charge-discharge cycle, the capacity faded from 218 mAh g^{-1} to 188 mAh g^{-1}, which was much larger than the following cycles as expected because of the SEI. From 2^{nd} cycle to the 20^{th} cycle, the coulombic efficiency (CE) was consistently high between 96% and 99%. On the 20^{th} cycle, the half cell maintained 88% of initial discharge capacity. The discharge capacities in the first, 5^{th}, 10^{th}, $15^{th}$and 20^{th} cycles are 188, 182, 175, 169 and 166 mAh g^{-1}, respectively.

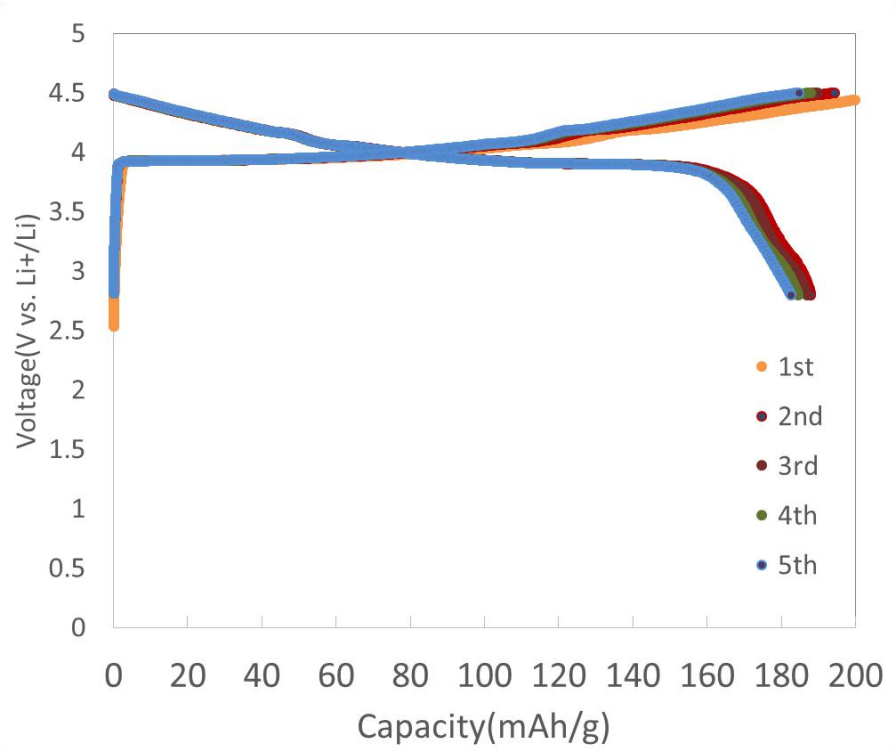

Figure 3.11. Voltage-capacity curves of the half-cell employing $LiCoO_2$:CB:PVDF=50:40:10 electrode as cathode between 2.5 and 4.5V vs. $V_{Li^+/Li}$ at C/5 rate.

The voltage and capacity curves of $LiCoO_2$:CB:PVDF=50:40:10 electrode as cathode half cell between 2.5 and 4.5V vs. $V_{Li^+/Li}$ at C/5 rate are presented in Figure 3.11. Two main plateaus were observed at 4V and 3.8V vs. Li/Li^+, corresponding with lithium ion extraction and insertion in $LiCoO_2$ cathode materials, which was in agreement with cyclic voltammetry characterization. The stability of the plateau indicates that the oxidation and reduction are fully reacting with lithium metal in half cell.

3.4 NiO/$LiCoO_2$ Full Cell Lithium Ion Batteries

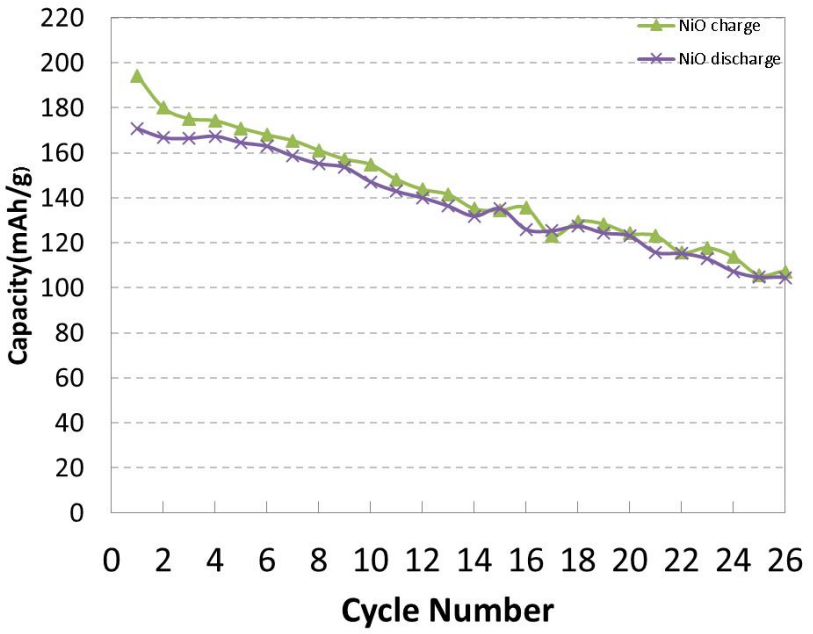

Figure 3.12. Capacity fade of the NiO/$LiCoO_2$ full cell employing NiO:CB:PVDF=50:40:10 anode and LCO:CB:PVDF=50:40:10 cathode between 1.2 and 4.2V vs. $V_{Li+/Li}$ at C/10 rate.

Figure 3.12 shows the capacity retention of the NiO/$LiCoO_2$ full cell employing NiO:CB:PVDF=50:40:10 anode and LCO:CB:PVDF=50:40:10 cathode between 1.2 and 4.2V vsVLi$^+$/Li at a rate of C/10. With initial cycling, the capacity only slightly decreased from 194 to 171 mAh g^{-1} with CE in the first cycle of 88%. After five cycles, the discharge capacity stabilized around 167 mAh g^{-1} with the CE stabilizing at 92.8%-96%. Nevertheless, the capacity decreased gradually from 164 to 135 mAh g^{-1} at C/10 rate from the 5th to 15th cycle. From the 15th to the 25th cycle, the steadily decreased slightly, which might be due to the continuous formation of the SEI layer in the NiO anode. Comparing with LCO's half cell performance in Figure 3.10, the full cell decline had a sharper slope. For the first 25 cycles, the full cell discharge capacity decreased from 170.7 to 107.3 mAh g^{-1} indicating faster capacity fade comparing with the cathode half cell's capacity fade from 188.0 to 154.7 mAh g^{-1}.

The lower performance might be due to the limited supply of lithium ions provided by the positive electrode and electrolyte during cycling, an increase in the resistance of components by additional SEI formation, or dissolution of the electrolyte and metals from the cathode.[19]

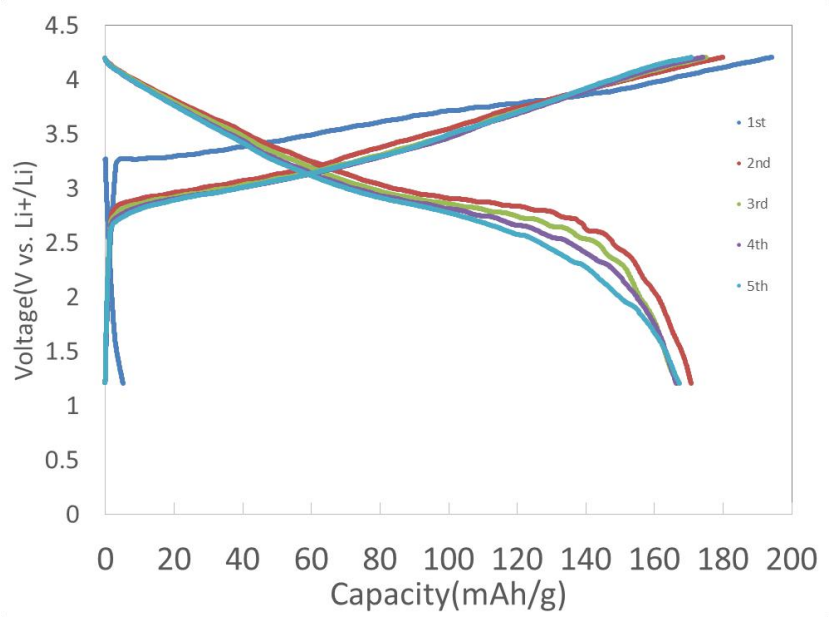

Figure 3.13. Voltage-capacity curves of the NiO/$LiCoO_2$ full cell employing NiO:CB:PVDF=50:40:10 anode and LCO:CB:PVDF=50:40:10 cathode between 1.2 and 4.2V vs. $V_{Li+/Li}$ at C/10 rate

Figure 3.13 presents the charge-discharge curves for the first five cycles of the NiO/$LiCoO_2$ full cell employing NiO:CB:PVDF=50:40:10 anode and LCO:CB:PVDF=50:40:10 cathode between 1.2 and 4.2V at C/10 rate. In the figure, two plateaus located around 3V and 2.5V were observed in all five cycles leading to charge and discharge capacity of 175 and 167 mAh g^{-1} separately. The charge processes for those five cycles all essentially overlap. However, the discharge curves do slightly shift at lower cell voltages between the 1st and the 5th cycle. When comparing with the LCO half cell charge-discharge curve in Figure 3.11, the full cell charge-discharge is significantly more sloped whereas the LCO half cell curve was essentially flat. The full cell's voltage plateaus declined by 1 V for both charge and

discharge process which is what would be expected given the discharge plateaus for pure NiO shown Figure 3.3.

3.5 G5/$LiCoO_2$ Full Cell Lithium Ion Batteries

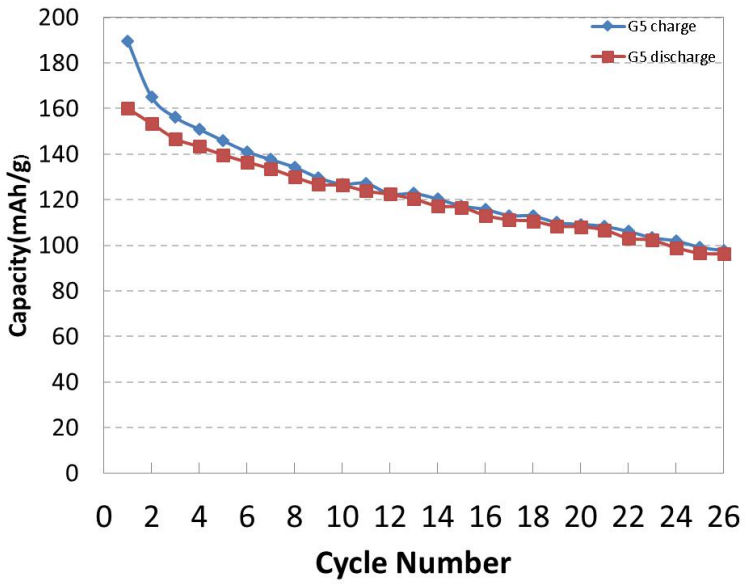

Figure 3.14. Capacity fade of the Graphite/$LiCoO_2$ full cell employing G5:CB:PVDF=50:40:10 anode and LCO:CB:PVDF=50:40:10 cathode between 0.01 and 4.2V vs. $V_{Li+/Li}$ at C/10 rate.

Figure 3.14 shows the cyclic behavior of a graphite/$LiCoO_2$ full cell with a G5:CB:PVDF=50:40:10 anode and LCO:CB:PVDF=50:40:10 cathode between 0.01 and 4.2V at a C/10 rate. The G5/LCO full cell capacity drops significantly even during the initial charge and discharge cycles from 189 to 160 mAh g^{-1} with CE of 84.6% which is supposed due to SEI formation. From then, the capacity reduced gradually to 99 mAh g^{-1} at the 25th cycle. However, the CE increased from 84.6% to 99.6% at the 10th cycle, and the CE stabilized around 98% at the 25th cycle.

Compared with anode and cathode half cell capacity retention, the full cell capacity fade was more like the cathode than the anode. Graphite and NiO anode half

cells had much better cycleability than LCO. As a result, the cathode capacity loss is probably the major reason for the observed full cell capacity fade.

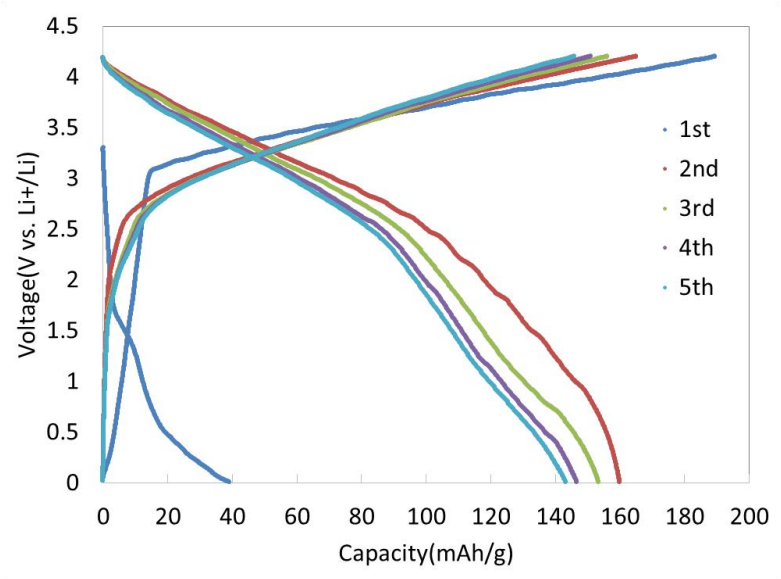

Figure 3.15. Voltage-capacity curves of the Graphite/$LiCoO_2$ full cell employing G5:CB:PVDF=50:40:10 anode and LCO:CB:PVDF=50:40:10 cathode between 0.01 and 4.2V vs. $V_{Li+/Li}$ at C/10 rate.

Figure 3.15 reports the voltage-capacity curves of the G5/$LiCoO_2$ full cell employing G5:CB:PVDF=50:40:10 anode and LCO:CB:PVDF=50:40:10 cathode between 0.01 and 4.2V at C/10 rate. The shape of curves are sloped for both charge and discharge processes in a fashion that is mostly similar with NiO/LCO full cell. The voltage plateau for lithium ion extraction and insertion appears at voltage 3V and 2.5V, which is also agree with the NiO/LCO full cell. When comparing with the NiO/LCO full cell, G5/LCO has voltage plateaus that are more sloped than flat. The flatness of voltage plateau is generally related with the reaction reversibility of the active materials.

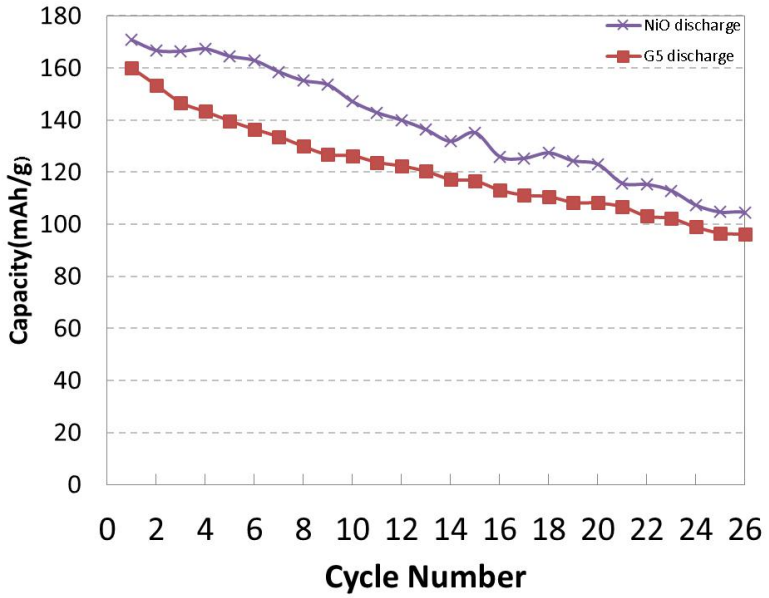

Figure 3.16. Comparison of discharge capacity fade of Graphite/$LiCoO_2$ and NiO/$LiCoO_2$ full cell employing G5:CB:PVDF=50:40:10, NiO:CB:PVDF=50:40:10 anode and LCO:CB:PVDF=50:40:10 cathode at C/10 rate.

Figure 3.16 compares the discharge capacity fade of Graphite/$LiCoO_2$ and NiO/$LiCoO_2$ full cells employing G5:CB:PVDF=50:40:10, NiO:CB:PVDF=50:40:10 anode and LCO:CB:PVDF=50:40:10 cathode at C/10 rate. This figure shows that the capacity of both full cells was essentially equivalent around 100 mAh g^{-1} remaining at the 25th cycle. The two full cells show similar degradation rates to Figure 3.10, which is likely due to the cathode capacity loss. NiO/LCO full cell has a slightly higher discharge capacity than G5/LCO, which was about 25 mAh g^{-1} during the first five cycles and 8 mAh g^{-1} around the 25th cycle. Regarding the full cell cycleability, the discharge capacity for the NiO/LCO full cell was pretty stable for the first five cycles. Then capacity faded slowly from the 5th to the 10th cycle, then the degradation rate increased from the 10th to the 15th cycle.

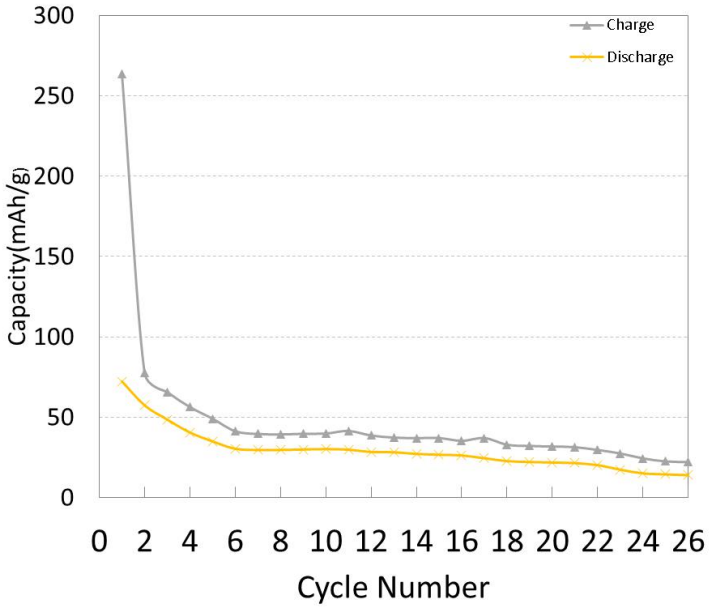

Figure 3.17. Capacity fade of the NiO/$LiCoO_2$ full cell employing NiO:CB:PVDF=50:40:10 anode and LCO:CB:PVDF=70:20:10 cathode between 2 and 4.2V $V_{Li+/Li}$ at C/5 rate.

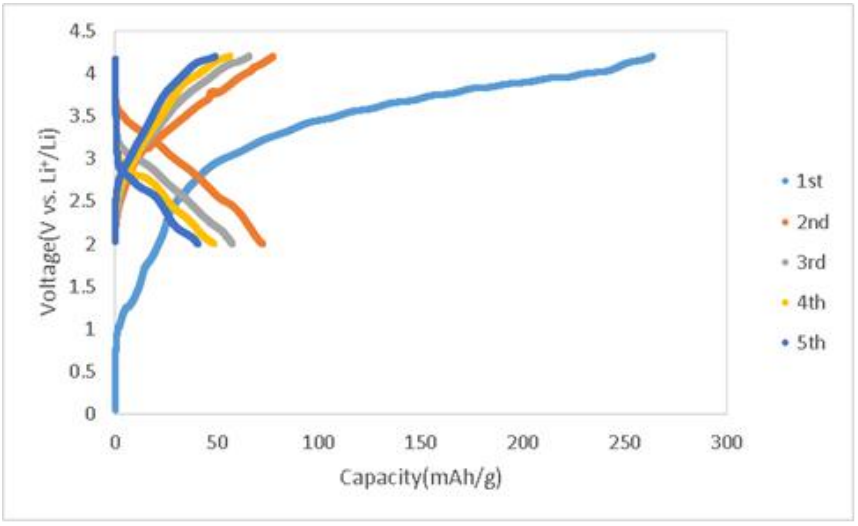

Figure 3.18. Voltage-capacity curves of the NiO/$LiCoO_2$ full cell employing NiO:CB:PVDF=50:40:10 anode and LCO:CB:PVDF=70:20:10 cathode between 2 and 4.2V vs. $V_{Li+/Li}$ at C/5 rate.

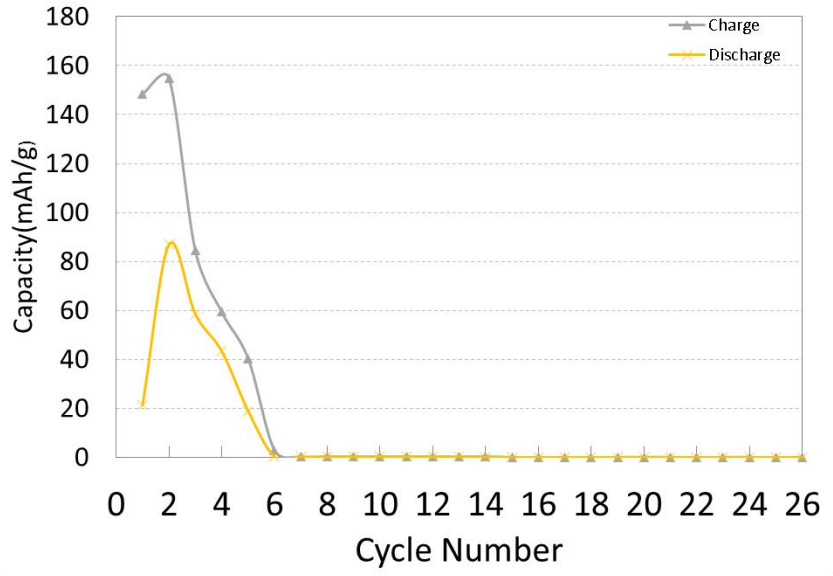

Figure 3.19. Capacity fade of the Graphite/$LiCoO_2$ full cell employing NiO:CB:PVDF=80:10:10 anode and LCO:CB:PVDF=70:20:10 cathode between 2 and 4.2V $V_{Li+/Li}$ at C/5 rate.

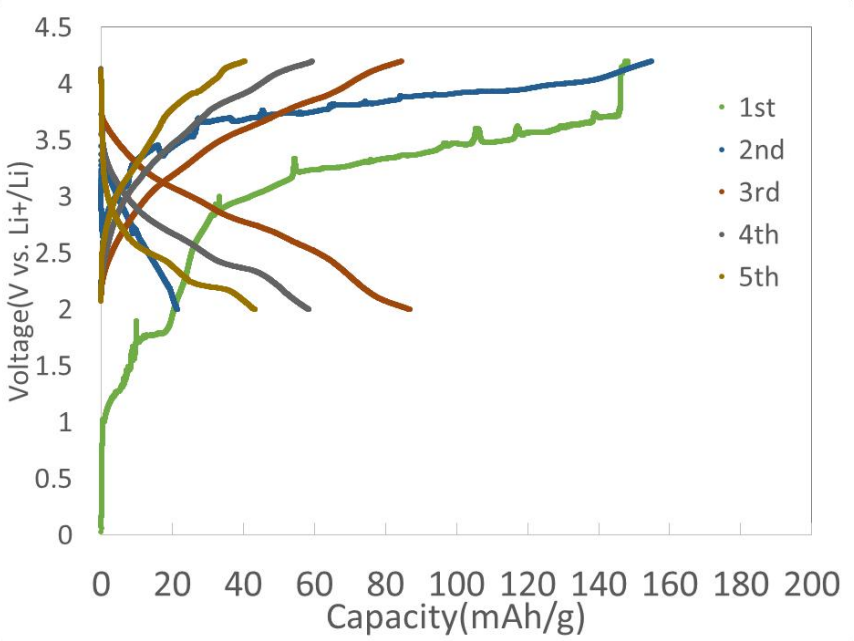

Figure 3.20. Voltage-capacity curves of the NiO/ $LiCoO_2$ full cell employing NiO:CB:PVDF=80:10:10 anode and LCO:CB:PVDF=70:20:10 cathode between 2 and 4.2V $V_{Li+/Li}$ at C/5 rate.

Figures 3.17-3.20 show the performance of NiO/LCO and G5/LCO full cells without capacity match, cut off voltage adjust and pre-lithiation. Figure 3.17 shows

the capacity fade of a NiO/$LiCoO_2$ full cell employing NiO:CB:PVDF=50:40:10 anode and LCO:CB:PVDF=70:20:10 cathode between 2 and 4.2V at C/5 rate. The first cycle showed a very significant irreversible capacity loss, which decreased the capacity from 263.6 to 72.3 mAh g^{-1}. Figure 3.19 shows the capacity fade of a NiO/$LiCoO_2$ full-cell employing NiO:CB:PVDF=80:10:10 anode and LCO:CB:PVDF=70:20:10 cathode obtained at a C rate of C/5 between 2 and 4.2V. Without capacity match which anode capacity is about 3 times higher than cathode capacity compared with above matched cell with 1.10:1 capacity ratio and application of appropriate cutoff voltage, the irreversible capacity loss was huge, and the full cell died after only 6 cycles. With 2V as the lower cutoff voltage, the NiO anode active materials likely could not charge completely, and they systematically consumed all of the Li contained in the cathode during the iniatial formation cycles, which might be the reason for such poor capacity retention.

These results illustrate the importance of several factors affecting full cell capacity and retention.

Chapter 4 Conclusions

In this thesis, the influence of conductivity NiO, G5 graphite and LCO on capacity retention in half cells has been explored. The NiO half cell performance demonstrated that better conductivity could help to improve the charge and discharge capacity by more than 100 mAh/g. The likely reason for this is that additional conductive carbon can influence the formation of the solid electrolyte interphase and allow for the accessibility of reactants because of higher electrode conductivity. The higher ratio of conductive carbon helps reduce the irreversible capacity loss resulting from SEI formation and protect structure damage. Moreover carbon also reduces the number of lithium ions that are wasted to SEI formation in full cell batteries. Additionally, increased conductivity could also reduce the effective lithium ion transfer distance. The shorter lithium ion transfer distance would reduce the mass transfer resistance during lithium ion lithiation and delithiation processes, which could also facilitate capacity retention. In summary, the most important factors for improving capacity retention in half cells are: conductivity, cut off voltage and charge/discharge rate.

Moreover, in this thesis, NiO/LCO full cell lithium ion batteries were assambled and their performance reported. The full cell with NiO anode and LCO cathode was tested between 1.2-4.2V under C/10 rate, which had more than 100 mAh/g capacity after 25 cycles. As comparison, graphite/LCO full cell LIBs were assembled and tested between 0.001-4.2V under C/10 rate. Higher conductivity significantly improved full cell capacity retention by 100 mAh/g. It was also shown that the NiO/LCO full cells had similar tendencies to G5/LCO full cells. In summary, the primary factors influencing the capacity and retention of full cells were: conductivity, cut off voltage, pre lithiuation and charge/discharge rate, and cell balance.

References

1. Yang, Z. *et al.* Electrochemical energy storage for green grid.pdf. *Chem. Rev.* 3577–3613 (2011).

2. Goodenough, J. B. & Park, K.-S. The Li-Ion Rechargeable Battery: A Perspective. *J. Am. Chem. Soc.* **135,** 1167–1176 (2013).

3. Crabtree, G. The energy-storage revolution. *Nat.* | *Outlook Energy Storage* **526,** S92 (2015).

4. air pollution china comparison - Google Search.

5. Dunn, B., Kamath, H. & Tarascon, J.-M. Electrical Energy Storage for the Grid: A Battery of Choices. *Science (80-.).* **334,** 928–935 (2011).

6. Specific power. **501,** 2008–2008 (2008).

7. Chen, Z. *R ep ro d u ced with p erm ission o f the copyright ow ner. Further reproduction prohibited w ithout perm ission.* (2003).

8. etvi.

9. M., H. & Fichtner, M. Magnesium Sulphide as Anode Material for Lithium-Ion Batteries. *Electrochim. Acta* **169,** 180–185 (2015).

10. Battery, M. L. Tandem Structure of Porous Silicon Film on Single-Walled Carbon Nanotube. **4,** 4683–4690 (2010).

11. Bhandavat, R. & Singh, G. Improved electrochemical capacity of precursor-derived Si (B) CN-carbon nanotube composite as Li-ion battery anode. *ACS Appl. Mater. Interfaces* **4,** 5092–5097 (2012).

12. Landi, B. J., Ganter, M. J., Cress, C. D., DiLeo, R. a. & Raffaelle, R. P. Carbon nanotubes for lithium ion batteries. *Energy Environ. Sci.* **2,** 638 (2009).

13. Gonz??lez, Z. *et al.* The influence of carbon nanotubes characteristics in their performance as positive electrodes in vanadium redox flow batteries. *Sustain. Energy Technol. Assessments* **9,** 105–110 (2015).

14. Lee, S. W. *et al.* High-power lithium batteries from functionalized carbon-nanotube electrodes. *Nat. Nanotechnol.* **5,** 531–537 (2010).

15. Choi, W. High Capacity and Excellent Stability of. *ACS Nano* **4,** 3440–3446 (2010).

16. Kang, C. *et al.* 3-dimensional carbon nanotube for Li-ion battery anode. *J. Power Sources* **219,** 364–370 (2012).

17. Bordes, A., Eom, K. & Fuller, T. F. The effect of fluoroethylene carbonate additive content on the formation of the solid-electrolyte interphase and capacity fade of Li-ion full-cell employing nano Si-graphene composite anodes. *J. Power Sources* **257,** 163–169 (2014).

18. Brutti, S. *et al.* A high power Sn–C/C–LiFePO4 lithium ion battery. *J. Power Sources* **217,** 72–76 (2012).

19. Eom, K., Joshi, T., Bordes, A., Do, I. & Fuller, T. F. The design of a Li-ion full cell battery using a nano silicon and nano multi-layer graphene composite anode. *J. Power Sources* **249,** 118–124 (2014).

20. Spinner, N., Zhang, L. & Mustain, W. E. Investigation of metal oxide anode degradation in lithium-ion batteries via identical-location TEM. *J. Mater. Chem. A* **2,** 1627 (2014).

21. Spinner, N. S. *et al.* Influence of conductivity on the capacity retention of NiO anodes in Li-ion batteries. *J. Power Sources* **276,** 46–53 (2015).

22. Spinner, N. & Mustain, W. E. Nanostructural effects on the cycle life and Li+ diffusion coefficient of nickel oxide anodes. *J. Electroanal. Chem.* **711,** 8–16 (2013).

23. Hu, S. *et al.* Effect of different binders on electrochemical properties of LiFePO4/C cathode material in lithium ion batteries. *Chem. Eng. J.* **237,** 497–502 (2014).

24. Beattie, S. D. *A STUDY OF ELECTRODEPOSITED NEGATIVE ELECTRODES FOR LITHIUM-ION BATTERIES*. (2004).

25. Zhu, X.-J., Hu, J., Dai, H.-L., Ding, L. & Jiang, L. Reduced graphene oxide and nanosheet-based nickel oxide microsphere composite as an anode material for lithium ion battery. *Electrochim. Acta* **64,** 23–28 (2012).

26. Cheng, M.-Y., Ye, Y.-S., Chiu, T.-M., Pan, C.-J. & Hwang, B.-J. Size effect of nickel oxide for lithium ion battery anode. *J. Power Sources* **253,** 27–34 (2014).

27. Hwang, B. J., Chen, C. Y., Cheng, M. Y., Santhanam, R. & Ragavendran, K. Mechanism study of enhanced electrochemical performance of ZrO2-coated LiCoO2 in high voltage region. *J. Power Sources* **195,** 4255–4265 (2010).

28. Yoon, Y. S., Lee, S. H., Cho, S. B. & Nam, S. C. Influence of Two-Step Heat Treatment on Sputtered Lithium Cobalt Oxide Thin Films. *J. Electrochem. Soc.* **158,** A1313 (2011).

29. Hammouda, B. Physical characterization methods. 1–64

30. Brutti, S. *et al.* A high power Sn–C/C–LiFePO4 lithium ion battery. *J. Power Sources* **217,** 72–76 (2012).

31. Veluri, P. S., Shaligram, A. & Mitra, S. Porous ??-Fe<inf>2</inf>O<inf>3</inf> nanostructures and their lithium storage properties as full cell configuration against

LiFePO<inf>4</inf>. *J. Power Sources* **293,** 213–220 (2015).

32. Wang, X., Hao, H., Liu, J., Huang, T. & Yu, A. A novel method for preparation of macroposous lithium nickel manganese oxygen as cathode material for lithium ion batteries. *Electrochim. Acta* **56,** 4065–4069 (2011).

33. Liu, Y.-H., Takasaki, T., Nishimura, K., Yanagida, M. & Sakai, T. Development of lithium ion battery using fiber-type lithium-rich cathode and carbon anode materials. *J. Power Sources* **290,** 153–158 (2015).

34. Zhang, W., Ma, G., Gu, H., Yang, Z. & Cheng, H. A new lithium-ion battery: CuO nanorod array anode versus spinel LiNi0.5Mn1.5O4 cathode. *J. Power Sources* **273,** 561–565 (2015).

35. Yuan, F. W. & Tuan, H. Y. Scalable solution-grown high-germanium-nanoparticle-loading graphene nanocomposites as high-performance lithium-ion battery electrodes: An example of a graphene-based platform toward practical full-cell applications. *Chem. Mater.* **26,** 2172–2179 (2014).

36. Reimers, J. N. & Dahn, J. R. Electrochemical and In. **139,** 2–8 (1992).

37. Mai, S., Xu, M., Liao, X., Xing, L. & Li, W. Improving cyclic stability of lithium nickel manganese oxide cathode at elevated temperature by using dimethyl phenylphosphonite as electrolyte additive. *J. Power Sources* **273,** 816–822 (2015).